cmgh
CELLULAR AND MOLECULAR GASTROENTEROLOGY AND HEPATOLOGY

ORIGINAL RESEARCH

Glycogen Synthase Kinase 3 β Hepatocyte Deletion Attenuates Ferroptosis and Metabolic Dysfunction-associated Steatohepatitis in Mice

Khaled Warasnhe,[1] Akitoshi Sano,[1,2] Qianqian Guo,[1] Nantawat Satthawiwat,[1,3,4] Xin Dai,[1,5] Peyton A. Classon,[1] Chady Meroueh,[6] Hyun Se Kim Lee,[1] Lucía Valenzuela-Pérez,[1] Stella Victorelli,[7] Adebowale O. Bamidele,[1,8] Petra Hirsova,[1] Davide Povero,[1] and Samar H. Ibrahim[1,9]

[1]Division of Gastroenterology and Hepatology, Mayo Clinic, Rochester, Minnesota; [2]Division of Gastroenterology, Tohoku University Graduate School of Medicine, Sendai, Japan; [3]Center of Excellence in Hepatitis and Liver Cancer, Chulalongkorn University, Bangkok, Thailand; [4]Department of Biochemistry, Medical Biochemistry Program, Faculty of Medicine, Chulalongkorn University, Bangkok, Thailand; [5]Department of Gastroenterology and Hepatology, Tianjin Medical University General Hospital, Tianjin, China; [6]Department of Anatomic Pathology, Mayo Clinic, Rochester, Minnesota; [7]Department of Physiology and Biomedical Engineering, Mayo Clinic, Rochester, Minnesota; [8]Department of Immunology, Mayo Clinic, Rochester, Minnesota; and [9]Division of Pediatric Gastroenterology and Hepatology, Mayo Clinic, Rochester, Minnesota

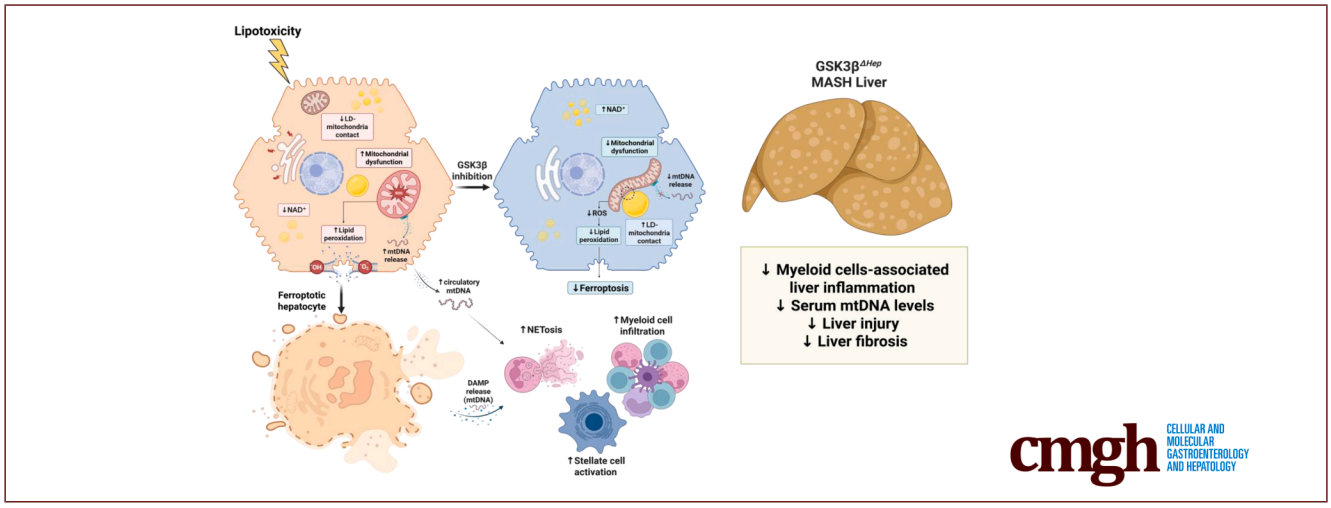

SUMMARY

Hepatocyte-specific *Gsk3β* knockout (*Gsk3β*$^{\Delta Hep}$) confers metabolic resilience in mice fed a metabolic dysfunction-associated steatohepatitis (MASH)-inducing diet, mainly by improving mitochondrial bioenergetics, liver NAD^+ levels, and mitochondria-lipid droplet contact. Furthermore, *Gsk3β*$^{\Delta Hep}$ mice fed MASH-inducing diets exhibited reduced liver injury, ferroptosis, release of damage-associated molecular patterns, such as mitochondrial DNA, hepatic myeloid cell infiltration, and fibroinflammatory response. Taken together, our data support the potential therapeutic role of GSK3β inhibition in human MASH.

BACKGROUND & AIMS: Metabolic dysfunction-associated steatohepatitis (MASH) is characterized by toxic lipid-induced cellular stress (lipotoxicity), which culminates in lethal and sublethal hepatocyte injury and a sterile

WHAT YOU NEED TO KNOW

Background: MASH is a progressive liver disease driven by mitochondrial dysfunction and inflammation. GSK3β is a key regulator of metabolic and cell death pathways in hepatocyte. Emerging evidence implicates aberrant GSK3β signaling in MASH pathogenesis, yet its hepatocyte-specific role remains unclear.

Impact: Hepatocyte-specific *Gsk3β* deletion in murine MASH improves mitochondrial function, enhances liver NAD^+ levels, and promotes mitochondria-lipid droplet contact, leading to reduced ferroptotic liver injury and fibroinflammatory responses.

Future directions: Future studies are needed to evaluate the therapeutic potential of hepatocyte-targeted GSK3β inhibition in human MASH.

fibroinflammatory response. We previously reported that pharmacological inhibition of glycogen synthase kinase 3 (GSK3) ameliorates murine MASH. However, the hepatocyte-specific role of GSK3β in lipotoxic injury and the fibroinflammatory response in MASH remains unclear.

METHODS: We generated hepatocyte-specific *Gsk3β* knockout (*Gsk3β*$^{\Delta Hep}$) mice by crossing *Gsk3β*$^{fl/fl}$ mice with albumin-Cre mice. Mice were fed either a choline-deficient high-fat diet (CDHFD) or a high-fat, fructose, and cholesterol (FFC) diet to induce MASH.

RESULTS: Metabolic parameters and hepatic lipidomic were similar between FFC-fed *Gsk3β*$^{\Delta Hep}$ and *Gsk3β*$^{fl/fl}$ mice. The NanoString Metabolic Pathways Panel on liver tissues showed upregulation of NAD, mitochondrial function, and oxidative phosphorylation signaling pathways in FFC-fed *Gsk3β*$^{\Delta Hep}$ mice compared with *Gsk3β*$^{fl/fl}$ mice. In vitro studies in palmitate-treated hepatocytes showed that mitochondrial morphology, biogenesis, contact with lipid droplets, and respiration were improved, whereas mitochondrial DNA release and Ferroptosis Suppressor Protein 1 (FSP1) phase separation were reduced with pharmacological GSK3 inhibition or in hepatocytes isolated from *Gsk3β*$^{\Delta Hep}$ mice. Similarly, liver injury, lipid peroxidation, ferroptosis markers, and circulating mitochondrial DNA levels were reduced in *Gsk3β*$^{\Delta Hep}$ mice with MASH. Furthermore, *Gsk3β*$^{\Delta Hep}$ mice with MASH had reduced hepatic expression of proinflammatory genes, myeloid cell infiltration, NETosis, and showed significant downregulation of fibrosis signaling pathways.

CONCLUSIONS: *Gsk3β*$^{\Delta Hep}$ reduced liver injury, mitochondrial DNA release, inflammation, and fibrosis in mice with MASH, secondary to improved mitochondrial bioenergetics and reduced ferroptosis. Therefore, GSK3β may be a potential therapeutic target for human MASH. *(Cell Mol Gastroenterol Hepatol 2026;20:101633; https://doi.org/10.1016/j.jcmgh.2025.101633)*

Keywords: Ferroptosis; Glycogen Synthase Kinase 3 β (GSK3β); Hepatocyte Injury; Inflammation; Liver Fibrosis; Metabolic Dysfunction-associated Steatohepatitis (MASH).

This article has an accompanying editorial.

Metabolic dysfunction-associated steatohepatitis (MASH) is a growing public health problem worldwide that has been linked to the obesity epidemic.[1] The pathogenesis of MASH involves both lipotoxicity (toxic lipid-induced cellular stress)[2] and a sterile inflammatory response paired with a dysfunctional reparative process that culminates in liver fibrosis.[3] The mechanisms by which hepatic inflammation evolves in MASH remain incompletely understood but appear to be linked to the proinflammatory microenvironment induced by lipotoxicity. Traditionally, lipotoxicity-induced cell death has been mainly attributed to apoptosis triggered by death receptors and endoplasmic reticulum (ER) stress.[4] Recently, other forms of cell death have been implicated in the pathogenesis of MASH, including necroptosis,[5] pyroptosis,[6] and ferroptosis.[7]

Ferroptosis is an increasingly recognized form of non-apoptotic programmed cell death involved in the pathogenesis of numerous inflammatory diseases.[8] Ferroptosis is characterized by the accumulation of lipid peroxides resulting from the iron-dependent peroxidation of polyunsaturated fatty acids (PUFAs) in membrane phospholipids. This process is primarily regulated by iron homeostasis and oxidative stress response.[9] The regulatory role of mitochondria in ferroptosis has recently been recognized, as mitochondria serve as a major source of intracellular reactive oxygen species (ROS) and are involved in maintaining iron homeostasis.[10] Additionally, lipid droplets (LDs) function as buffers against lipotoxic stress by sequestering excess fatty acids (FAs), particularly PUFAs, which induce ferroptosis. The buffering

Abbreviations used in this paper: **Acsl4, acyl-CoA synthetase long-chain family member 4; ALT, alanine aminotransferase; AMPK, AMP-activated protein kinase; ANOVA, analysis of variance; AR, aspect ratio; AT, adipose tissue; α-SMA, alpha-smooth muscle actin; Braf, Braf transforming gene; BSA, bovine serum albumin; Ccl2, C-C motif chemokine ligand 2; Ccr2, C-C chemokine receptor type 2; CDHFD, choline-deficient high-fat diet; Chop, C/EBP homologous protein; CitH3, citrullinated histone 3; CLAMS, Comprehensive Laboratory Animal Monitoring System; CoQ, Coenzyme Q; CV, central vein; CXCL2, C-X-C motif chemokine ligand 2; CYP2F2, cytochrome P450 family 2 subfamily f member 2; DAB, diaminobenzidine; DAMPs, damage-associated molecular patterns; DAPI, 4′,6-diamidino-2-phenylindole; DHODH, dihydroorotate dehydrogenase; DMEM, Dulbecco's modified Eagle's medium; DMSO, dimethyl sulfoxide; E, embryonic day; ECAR, extracellular acidification rate; ECL, enhanced chemiluminescence; ELISA, enzyme-linked immunosorbent assay; EM, electron microscopy; ER, endoplasmic reticulum; FA, fatty acids; FBS, fetal bovine serum; Fer-1, Ferrostatin-1; FFA, free fatty acid; FFC, fat; fructose, and cholesterol; Fsp1, ferroptosis suppressor protein 1; Fth1, ferritin heavy polypeptide 1; G6pc, glucose 6 phosphatase catalytic subunit 1; GAPDH, glyceraldehyde-3-phosphate dehydrogenase; GO, Gene Ontology; GP, Gaussian process; GPD2, glycerol-3-phosphate dehydrogenase 2; GPX4, glutathione peroxidase 4; GS, glutamine synthase; GSK3β, glycogen synthase kinase 3 β; HOMA-IR, Homeostatic Model Assessment for Insulin Resistance; H&E, hematoxylin and eosin; 4-HNE, 4-hydroxy-2-nonenal; HRP, horseradish peroxidase; IACUC, Institutional Animal Care and Use Committee; ING, 9-ING-41; IPA, Ingenuity Pathway Analysis; LD, lipid droplet; Lox, lysyl oxidase; LY, LY2090314; MASLD, metabolic dysfunction-associated steatotic liver disease; MASH, metabolic dysfunction-associated steatohepatitis; MCD, methionine and choline-deficient; MDA, malondialdehyde; MPO, myeloperoxidase; mPTP, mitochondrial permeability transition pore; MRI, magnetic resonance imaging; mRNA, messenger RNA; MTBE, methyl tertiary-butyl ether; mtDNA, mitochondrial DNA; MUFAs, mono-saturated fatty acids; NAD$^+$, nicotinamide adenine dinucleotide; NAFLD, nonalcoholic fatty liver disease; NAMPT, nicotinamide phosphoribosyl transferase; NAS, NAFLD activity score; NEFA, nonesterified free fatty acids; NET, neutrophil extracellular trap; NF-kB, nuclear factor kappa B; NPC, nonparenchymal cell; Nrf2, nuclear factor erythroid 2-related factor 2; OCR, oxygen consumption rate; Opa1, optic atrophy 1; oxPAPC, oxidized 1-palmitoyl-2-arachidonoyl-sn-glycero-3-phosphorylcholine; OxPLs, oxidized phospholipids; PA, palmitate; PAGE, polyacrylamide gel electrophoresis; PBS, phosphate-buffered saline; Pgc1a, peroxisome proliferator-activated receptor gamma coactivator 1-alpha; PI, propidium iodide; Plin5, perilipin 5; PMH, primary mouse hepatocyte; PRDX3, peroxiredoxin 3; Ptgs2, prostaglandin-endoperoxide synthase 2; PUFA, polyunsaturated fatty acids; PV, portal vein; RIPA, radioimmunoprecipitation assay; ROS, reactive oxygen species; RT-qPCR, real-time quantitative reverse transcription polymerase chain reaction; Scd1, stearyl-CoA desaturase 1; SDS, sodium dodecyl sulfate; SD, standard deviation; Serpine1, plasminogen activator inhibitor-1; SPLICs, split-GFP-based contact site sensor; Srebf1, sterol regulatory element binding transcription factor 1; TBST, Tris-buffered saline with 0.1% Tween-20; TEM, transmission electron microscopy; Tfam, mitochondrial transcription factor A; TFRC, transferrin receptor 1; TG, triglyceride; Thbs1, thrombospondin-I; Tlr7, toll-like receptor 7; TNF-α, tumor necrosis factor α.**

Most current article

2352-345X
https://doi.org/10.1016/j.jcmgh.2025.101633

capacity of LDs reduces the availability of PUFAs for lipid peroxidation, thereby preventing ferroptotic cell death.[11] In addition to their classical function as lipid reservoirs, LDs interact with other organelles, including mitochondria, to regulate FA trafficking and metabolism. The interaction between LDs and mitochondria plays a crucial role in transporting FAs from LD to mitochondria for subsequent oxidation and energy generation. LD-associated mitochondria in the liver exhibit higher metabolic fitness and FA oxidation capacity than cytoplasmic mitochondria, and this capacity is compromised in metabolic dysfunction-associated fatty liver disease (MASLD).[12] Under lipotoxic conditions, mitochondrial-LD spatial proximity is likely to reduce the availability of cytoplasmic FAs by increasing their trafficking to LDs,[13,14] suggesting that LD-mitochondrial contact may modulate lipotoxicity-induced ferroptosis in MASH. However, the cellular and molecular mediators of ferroptosis in MASH remain to be elucidated.

The inflammatory response in MASH is mainly mediated by the recruitment of proinflammatory myeloid cells.[15] Ferroptosis is involved in immune cell activation through the release of damage-associated molecular patterns (DAMPs), including mitochondrial DNA, cytokines, chemokines, and other mediators.[16] However, it remains unclear whether hepatocyte ferroptosis contributes to the proinflammatory response in MASH.

Glycogen synthase kinase 3β (GSK3β) is a master kinase that acts as a major hub linking numerous signaling pathways, including those involved in cell metabolism, adhesion, and inflammation.[17] Aberrant GSK3β activation is pathogenic in numerous inflammatory diseases, and GSK3β inhibitors have been successful in curtailing exuberant inflammatory responses in several rodent models.[18,19] GSK3β has been implicated in the regulation of ferroptosis in cancer.[20,21] In addition, GSK3β plays an important role in regulating mitochondrial bioenergetics in the brain.[22] We previously reported that pharmacological inhibition of GSK3 ameliorated liver injury, inflammation, and fibrosis, mainly by reducing the hepatic infiltration of recruited myeloid cells in murine MASH.[23] However, the role of GSK3β in hepatocyte mitochondrial dysfunction and ferroptosis in MASH is unclear. To address these knowledge gaps, we generated hepatocyte-specific *Gsk3β* knockout mice to dissect the cell-autonomous functions of GSK3β in MASH. Herein, we report that hepatocyte-specific *Gsk3β* knockout reduces liver injury, ferroptosis markers, myeloid cell-associated liver inflammation, and fibrosis in murine MASH. Furthermore, GSK3β genetic or pharmacological inhibition in vitro restored mitochondrial bioenergetics and increased mitochondrial LD contacts and LD-associated mitochondria in hepatocytes exposed to lipotoxic stress. These findings suggest that GSK3β plays a major role in hepatocyte ferroptosis and the proinflammatory response in MASH.

Results

Hepatocyte Gsk3β Deletion Does Not Alter the Metabolic Phenotypes in Diet-induced Murine MASH

To model human MASH in mice, we employed 2 distinct dietary models.[24] In the FFC diet model, mice are fed a Western diet high in fat, fructose, and cholesterol (FFC) for 24 weeks. The FFC model closely phenocopies human MASH and metabolic syndrome.[25–27] In the CDHFD model (A06071302, Research Diet)[27,28] mice are fed a choline-deficient, L-amino acid-defined, high-fat diet (CDHFD) for 6 weeks. The CDHFD model possesses all hepatic features of human MASH with more pronounced liver fibrosis and inflammation than the FFC model; however, mice on CDHFD do not develop obesity. To assess the effect of $Gsk3\beta^{\Delta Hep}$ on MASH-associated metabolic phenotypes, we fed $Gsk3\beta^{\Delta Hep}$ mice either a CDHFD (Figure 1*A*) or FFC diet (Figure 2*A*). The deletion of *Gsk3β* in hepatocytes was confirmed by Western blotting of isolated primary mouse hepatocytes. Western blot analysis of GSK3β in nonparenchymal cells (NPCs) showed comparable expression levels between $Gsk3\beta^{\Delta Hep}$ and $Gsk3\beta^{fl/fl}$ mice, confirming hepatocyte-specific deletion (Figure 1*B*). $Gsk3\beta^{\Delta Hep}$ mice on the MASH-inducing CDHFD exhibited similar metabolic parameters (body weight, liver/body weight ratio, and epididymal adipose tissue weight) as $Gsk3\beta^{fl/fl}$ mice on the same diet (Figure 1*C*). Similarly, FFC-fed $Gsk3\beta^{\Delta Hep}$ and $Gsk3\beta^{fl/fl}$ mice presented similar metabolic parameters (Figure 2*B*). Fasting blood glucose levels and Homeostatic Model Assessment of Insulin Resistance (HOMA-IR) results were similar in CDHFD-fed (Figure 1*D*) and FFC-fed (Figure 2*C*) $Gsk3\beta^{\Delta Hep}$ mice compared with those in $Gsk3\beta^{fl/fl}$ mice fed the same diet. Histological assessment suggested smaller LD size in the pericentral areas of $Gsk3\beta^{\Delta Hep}$ mice with the CDHFD diet-induced MASH (Figure 1*E*), and to a lesser extent in the FFC diet-induced MASH (Figure 2*D*). This observation was validated by machine learning-based zonal quantification of steatosis, which confirmed smaller LDs in the pericentral area of CDHFD-fed $Gsk3\beta^{\Delta Hep}$ mice compared with $Gsk3\beta^{fl/fl}$ mice (Figure 1*F*). No significant difference was observed in the steatosis score or steatosis percentage among the hepatic zones in CDHFD-fed (Figure 1*G*) and FFC-fed (Figure 2*E*) $Gsk3\beta^{\Delta Hep}$ mice compared with $Gsk3\beta^{fl/fl}$ mice. CDHFD-fed $Gsk3\beta^{\Delta Hep}$ mice demonstrated a significant reduction in nonalcoholic fatty liver disease (NAFLD) Activity Score (NAS), mostly secondary to reduced inflammation (Figure 1*E*). These findings were further supported by hepatic triglyceride (TG) measurements, which were comparable between MASH-inducing diet-fed $Gsk3\beta^{\Delta Hep}$ and $Gsk3\beta^{fl/fl}$ mice, indicating no significant differences in the quantitative assessment of hepatic steatosis in CDHFD-fed (Figure 1*H*) and FFC-fed mice (Figure 2*F*). To further examine the role of GSK3β in lipid metabolism and the liver composition of nonesterified free fatty acids (NEFA) and total FAs, we performed lipidomic analysis of liver tissue and identified a similar lipid composition between $Gsk3\beta^{\Delta Hep}$ and $Gsk3\beta^{fl/fl}$ mice (Figure 3*A*). Furthermore, a Comprehensive Laboratory Animal Monitoring System (CLAMS) study revealed no alterations in the metabolic rate, physical activity, respiratory quotient, or lean/fat mass ratio in FFC-fed $Gsk3\beta^{\Delta Hep}$ and $Gsk3\beta^{fl/fl}$ mice (Figure 3*B*).

Because GSK3β negatively regulates Wnt/β-catenin signaling, which is a critical player in liver metabolic zonation,[29] we assessed alterations in hepatic zonation in $Gsk3\beta^{\Delta Hep}$ and $Gsk3\beta^{fl/fl}$ mice by immunostaining for the

pericentral glutamine synthase (GS) and periportal cytochrome P450 family 2 subfamily f member 2 (CYP2F2) zonation markers. GS+ and CYP2F2+ areas were comparable between *Gsk3β*$^{\Delta Hep}$ and *Gsk3β*$^{fl/fl}$ mice, with no observable alterations in staining patterns (Figure 4*A*). Interestingly, the periportal CYP2F2+ area was reduced by the CDHFD in *Gsk3β*$^{fl/fl}$ mice and restored in *Gsk3β*$^{\Delta Hep}$ mice on the same diet, suggesting restoration of periportal

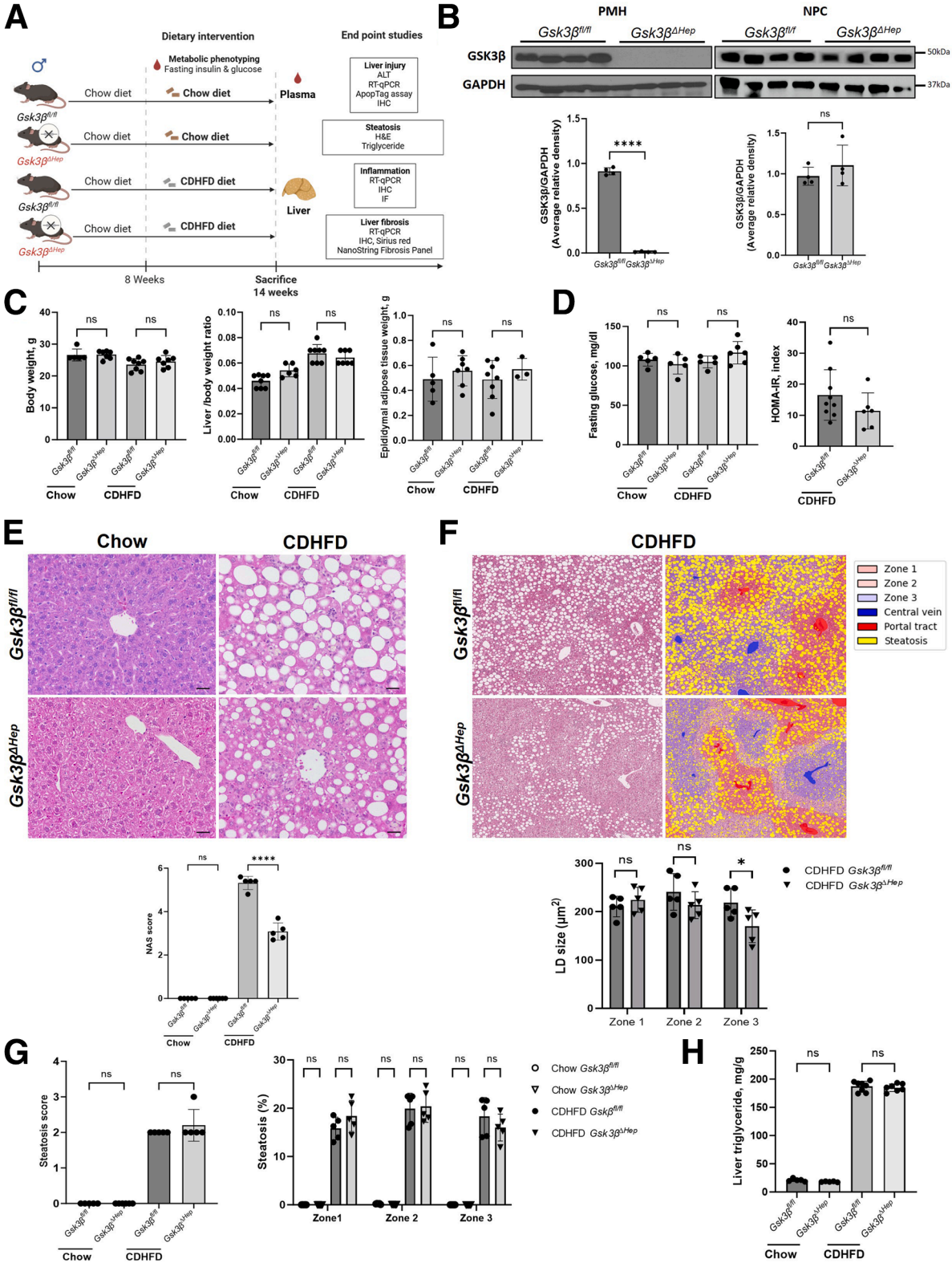

metabolic capacity in *Gsk3β*$^{\Delta Hep}$ mice (Figure 4*B*). Taken together, these results suggest that deletion of *Gsk3β* in hepatocytes in mice with diet-induced MASH reduces LD size in the pericentral area without altering hepatic triglyceride levels, lipid species composition, or gross metabolic phenotype.

Hepatocyte Gsk3β Inhibition Ameliorates Mitochondrial Function and Morphology in Lipotoxicity and Murine MASH

To further delineate the metabolic pathways altered in *Gsk3β*$^{\Delta Hep}$ mice, we performed a NanoString Metabolic Pathways Panel on liver tissue samples from FFC- and chow diet-fed *Gsk3β*$^{\Delta Hep}$ and *Gsk3β*$^{fl/fl}$ mice. Metabolic profiling of 768 genes identified 32 differentially expressed genes between FFC-fed *Gsk3β*$^{\Delta Hep}$ and *Gsk3β*$^{fl/fl}$ mice based on a *P* value threshold of $\leq .05$ (Figure 5*A*). Gene expression analysis revealed the upregulation of glucose 6 phosphatase catalytic subunit 1 (*G6pc)*, a key regulator of glucose homeostasis, and sterol regulatory element binding transcription factor 1 (*Srebf1*), a central transcription factor regulating lipid metabolism, and its downstream target stearyl-CoA desaturase 1 (*Scd1*) in FFC-fed *Gsk3β*$^{\Delta Hep}$ mice compared with that in *Gsk3β*$^{fl/fl}$ mice (Figure 5*A, B*), whereas Braf transforming gene (*Braf)* and toll-like receptor 7 (*Tlr7)* were downregulated (Figure 5*A, C*). Braf activation increases the accumulation of long-chain PUFAs and formation of LDs,[30] whereas TLR7 activation enhances the expression of proinflammatory cytokines, such as tumor necrosis factor α (TNF-α) and type I interferons, exacerbating liver inflammation and steatosis.[31] To further verify the NanoString analysis findings, we confirmed the top upregulated gene expression using real-time quantitative reverse transcription polymerase chain reaction (RT-qPCR) (Figure 5*D*). To explore the biological functions associated with the differentially expressed genes identified in FFC-fed *Gsk3β*$^{\Delta Hep}$ mice, we performed Ingenuity Pathway Analysis (IPA) and identified 45 canonical pathways that were differentially regulated in *Gsk3β*$^{\Delta Hep}$ mice (z-score $> \pm 2.0$ and $P < .05$). Importantly, among these pathways, nicotinamide adenine dinucleotide (NAD^+) signaling pathway was enriched (Figure 5*E*), whereas MASLD and nuclear factor kappa B (NF-kB) signaling pathways were downregulated (Figure 5*F*). Furthermore, Gene Ontology (GO) enrichment analysis using ShinyGO (v0.80) identified significant enrichment of biological pathways related to metabolic pathways, including the citrate cycle (TCA) and AMP-activated protein kinase (AMPK) signaling pathways in FFC-fed *Gsk3β*$^{\Delta Hep}$ mice compared with *Gsk3β*$^{fl/fl}$ mice (Figure 5*G*). Measurement of NAD^+ levels in whole liver tissue identified a significant increase in NAD^+ levels in FFC-fed *Gsk3β*$^{\Delta Hep}$ mice compared with that in *Gsk3β*$^{fl/fl}$ mice (Figure 5*I*). To further validate the upregulation of the NAD^+ signaling pathway, we examined the activity and expression of Nampt, the key enzyme in the NAD^+ salvage pathway, in our model. Immunostaining identified prominent nuclear and cytosolic expression of Nampt in the pericentral zone within the livers of *Gsk3β*$^{\Delta Hep}$ mice fed the MASH-inducing diet (Figures 6*A* and 7*A*). Interestingly, increased pericentral Nampt expression coincided with reduced steatosis in the pericentral zones of MASH diet-fed *Gsk3β*$^{\Delta Hep}$ mice. Mining of publicly available spatial proteomic data across hepatic zones revealed that Nampt expression does not follow a zonal pattern under baseline conditions.[32] Thus, *Gsk3β* deletion in hepatocytes seems to restore Nampt expression in the pericentral zones in mice fed the MASH-inducing diet, suggesting that the reduced pericentral hepatic steatosis in *Gsk3β*$^{\Delta Hep}$ mice with MASH is likely secondary to improved Nampt activity, given the known link between reduced Nampt activity and the development of hepatic steatosis.[33,34] Taken together, these analyses suggest that *Gsk3β*$^{\Delta Hep}$ mice fed a MASH-inducing diet have improved hepatic mitochondrial bioenergetics, oxidative phosphorylation, and substrate utilization, with reduced proinflammatory signaling.

To functionally confirm the unbiased in vivo observation using an in vitro system of lipotoxicity and understand the effect of GSK3β deletion on hepatocyte mitochondrial respiration, we assessed changes in the oxygen consumption rate (OCR) by conducting a mitochondrial stress test using a Seahorse XF analyzer. Our data indicated that OCR was significantly reduced in palmitate (PA)-treated *Gsk3β*$^{fl/fl}$ primary mouse hepatocytes (PMHs) compared with PA-treated *Gsk3β*$^{\Delta Hep}$ PMH. Specifically, PA-treated *Gsk3β*$^{\Delta Hep}$ PMHs showed higher maximal respiration and spare respiratory capacity than PA-treated *Gsk3β*$^{fl/fl}$ PMH (Figure 8*A*), supporting our NanoString-based messenger RNA (mRNA) profiling data that *Gsk3β* deletion promotes mitochondrial function in MASH. Bioenergetic analysis of the mouse hepatocyte cell line AML12 was performed to mechanistically corroborate our observations in PMH. In

Figure 1. (***See previous page***). **Hepatocyte-specific *Gsk3β* deletion in CDHFD-induced murine MASH does not alter the metabolic phenotype.** Hepatocyte-specific *Gsk3β* knockout (*Gsk3β*$^{\Delta Hep}$) mice were generated by crossing *Gsk3β* $^{fl/fl}$ with Alb-Cre mice. Eight-week-old *Gsk3β*$^{\Delta Hep}$ and *Gsk3β* $^{fl/fl}$ mice were fed either chow or CDHFD for 6 weeks to induce MASH development. (*A*) Schematic representation of the mouse model and feeding studies. (*B*) Western blot analysis of GSK3β protein levels to validate knockout efficiency (n = 4 per group). (*C*) Body weight, liver/body weight ratio, and epididymal adipose tissue weight (n = 5–10 per group). (*D*) Fasting glucose (mg/dL) and HOMA-IR (n = 5–10 per group). (*E*) Representative H&E-stained liver sections from chow- and CDHFD-fed *Gsk3β*$^{\Delta Hep}$ and *Gsk3β* $^{fl/fl}$ mice. NAS score (*bottom panel*) (n = 5 per group). (*F*) Representative images of machine learning-based steatosis quantification. Quantification of LD size (μm^2) in the hepatic zones (*bottom panel*). (*G*) Machine-learning-based quantification of the steatosis score and steatosis percentage in the hepatic zones (n = 5 per group). (*H*) Quantification of hepatic TG levels (n = 5–8 per group). Bar graphs represent the mean ± SD; **P* < .05, **** *P* < .0001, ns, nonsignificant (one-way ANOVA with Bonferroni's multiple comparison and unpaired *t*-test). Scale bar: 20 μm (*E*).

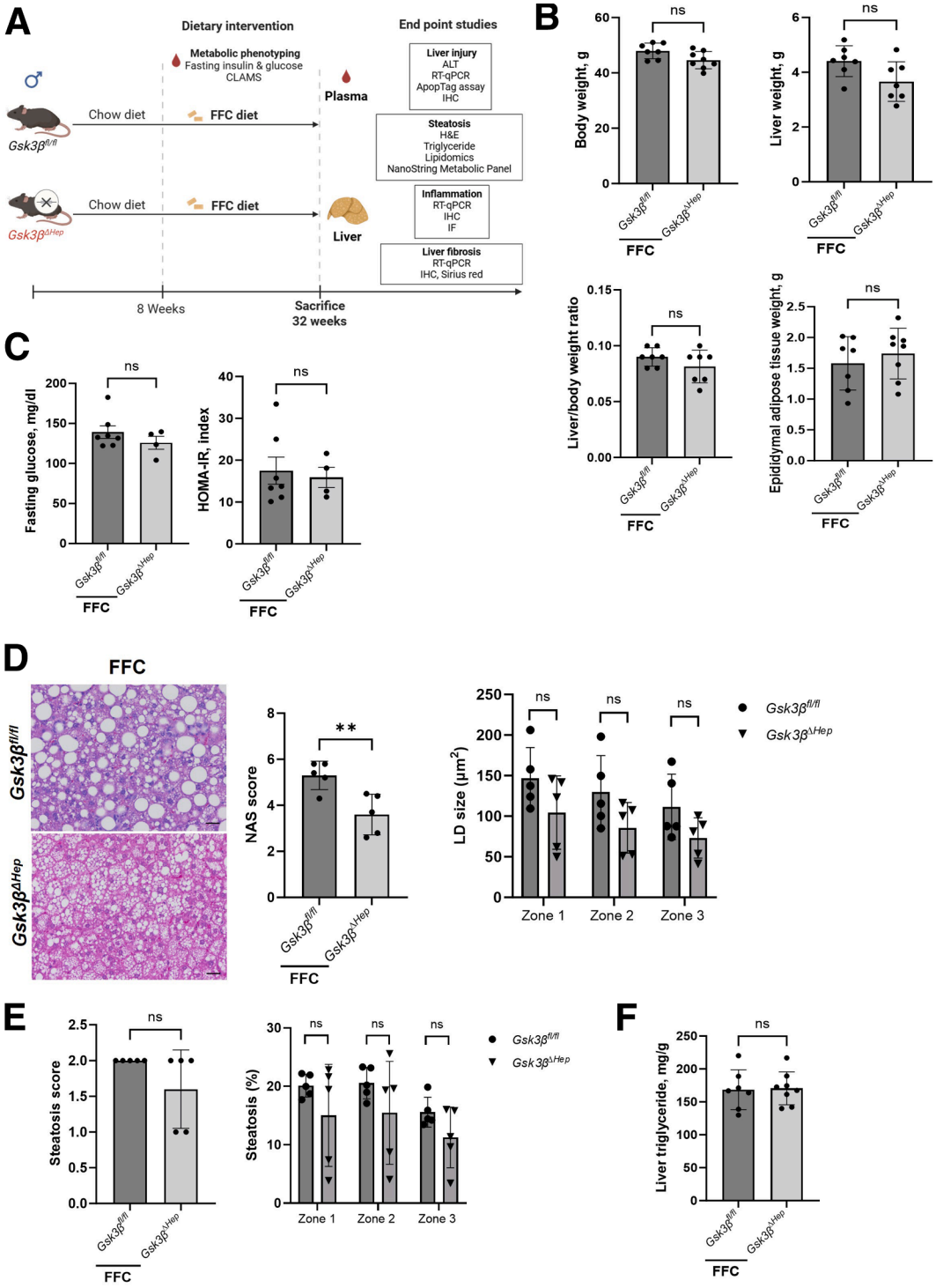

Figure 2. *Gsk3β* hepatocyte deletion in mice with FFC-induced MASH does not alter the metabolic phenotype. Eight-week-old *Gsk3β*$^{\Delta Hep}$ mice and *Gsk3β* $^{fl/fl}$ mice were fed either a chow or FFC diets for 24 weeks to induce MASH. (*A*) Schematic representation of the mouse model and the feeding study. (*B*) Body weight, liver weight, liver/body weight ratio, and epididymal adipose tissue weight (n = 7–8 per group). (*C*) Fasting glucose (mg/dL) and HOMA-IR (n = 4–7 per group). (*D*) Representative H&E-stained liver sections from the FFC-fed *Gsk3β*$^{\Delta Hep}$ mice and *Gsk3β* $^{fl/fl}$ mice (*left panel*). NAS score and quantification of LD size (μm^2) in the hepatic zones (*right*) (n = 5 per group). (*E*) Machine learning-based steatosis score and steatosis percentage in the hepatic zones (n = 5 per group). (*F*) Quantification of hepatic triglyceride levels (n = 7–8 per group). Bar graphs represent mean ± SD, ** $P < .01$, ns, non-significant (unpaired *t*-test). Scale bar: 20 μm (*D*).

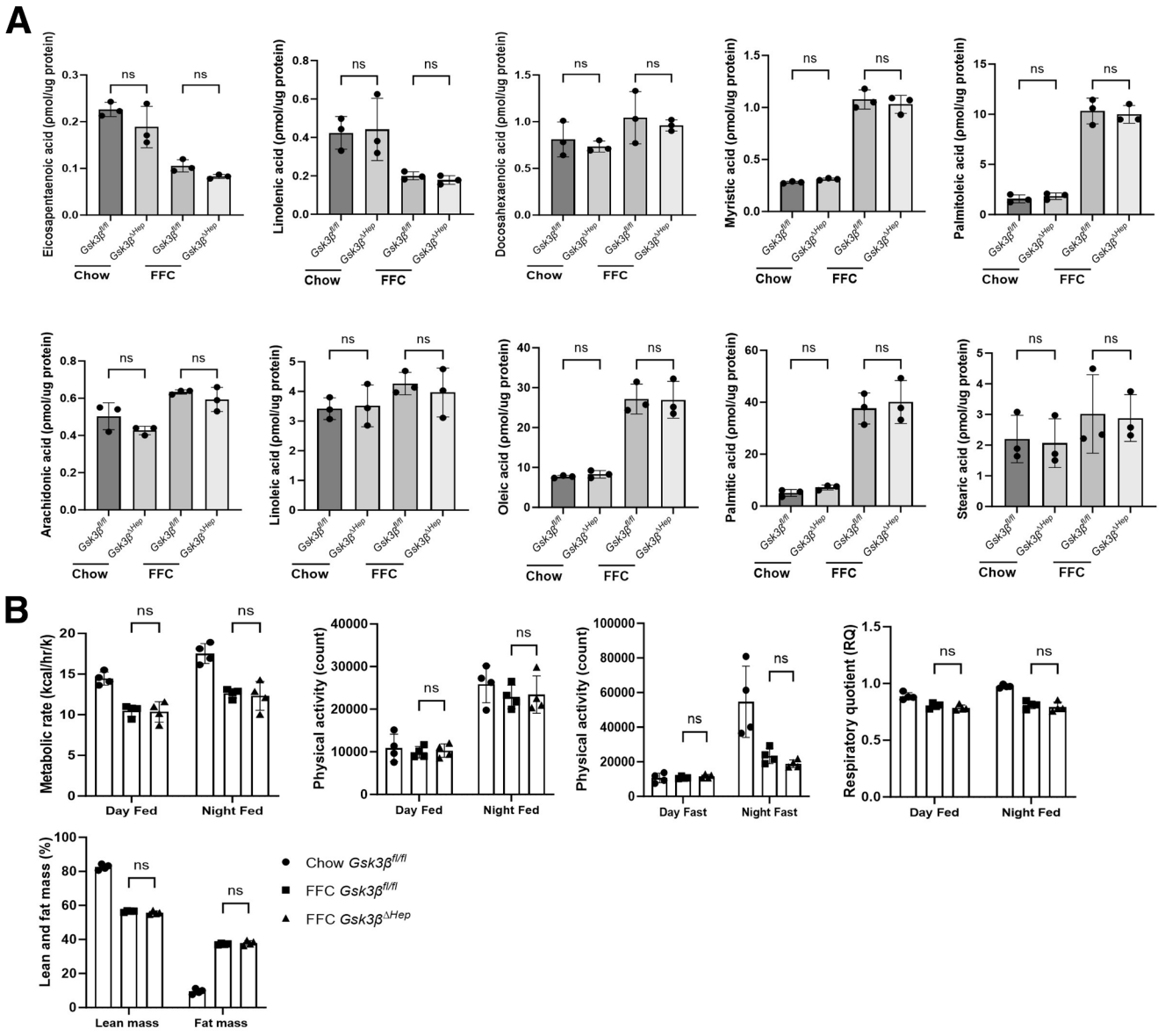

Figure 3. *Gsk3β* hepatocyte deletion did not alter the lipidomic profile or metabolic phenotype in mice with FFC-induced MASH. (*A*) Lipidomic profiling of liver samples from chow- and FFC-fed *Gsk3β*$^{\Delta Hep}$ mice vs *Gsk3β* $^{fl/fl}$ mice, with lipid levels normalized to protein content (n = 3 per group). (*B*) Metabolic rate, physical activity, normalized respiratory quotient assessed using the CLAMS study, and lean vs fat mass body composition measured using Echo-MRI (n = 4 per group). Bar graphs represent the mean ± SD; ns, nonsignificant (1-way ANOVA with Bonferroni's multiple comparison).

agreement with our bioenergetic studies in mouse primary hepatocytes, PA decreased OCR levels associated with basal respiration, ATP production, and maximal respiration in AML12 cells, whereas pharmacological inhibition of GSK3*β* enzymatic activity with LY2090314 (LY) restored maximal respiration and spare respiratory capacity (Figure 8*B*). In accordance, liver tissues of *Gsk3β*$^{\Delta Hep}$ mice showed higher mRNA expression of mitochondrial biogenesis genes, including mitochondrial transcription factor A (*Tfam*), peroxisome proliferator-activated receptor gamma coactivator 1-alpha (*Pgc1a*), optic atrophy 1 (*Opa1*), and nuclear factor erythroid 2-related factor 2 (*Nrf2*), than those of *Gsk3β*$^{fl/fl}$ mice (Figure 8*C*).

As mitochondrial morphology can be indicative of mitochondrial respiration and function,[35] we performed electron microscopy (EM) of liver tissues from chow- and FFC-fed mice to evaluate mitochondrial morphology. Circularity and aspect ratio (AR) are valuable parameters in EM-based quantification of mitochondrial morphology, as they provide insights into the structural and functional dynamics of mitochondria.[36] EM-based quantification of mitochondrial morphology showed lower circularity and higher AR, indicating more elongated or tubular mitochondria in FFC-fed *Gsk3β*$^{\Delta Hep}$ mice than in *Gsk3β*$^{fl/fl}$ mice (Figure 9*A, B*). Given the improved mitochondrial bioenergetics observed in our model, we examined LD-

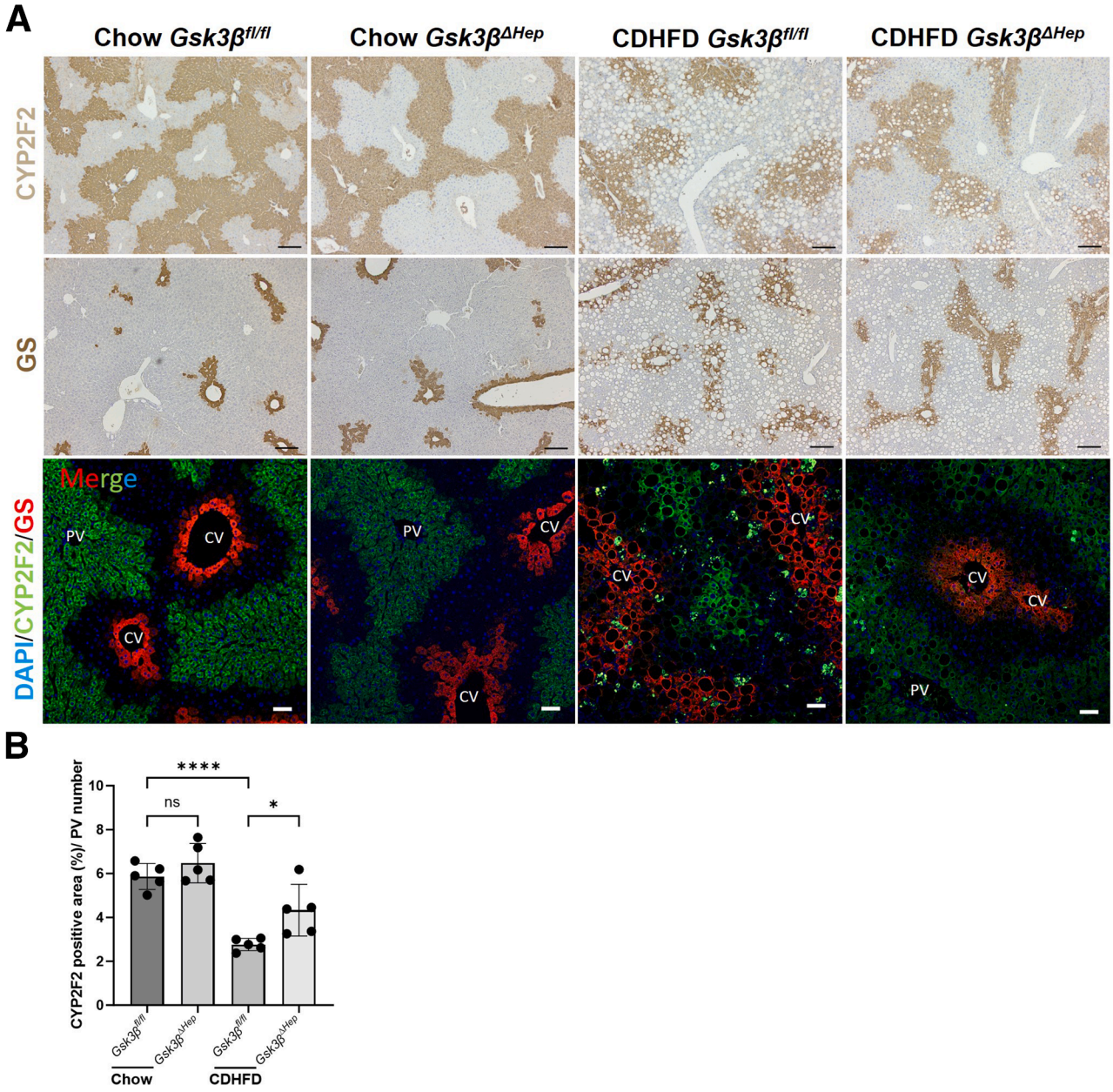

Figure 4. *Gsk3β* hepatocyte deletion in CDHFD-induced MASH mice did not alter zonation patterns. (*A*) Immunohistochemical (IHC) and immunofluorescence (IF) staining for the zonation markers CYP2F2 (periportal) and GS (pericentral) in liver sections from chow- and CDHFD-fed *Gsk3β*$^{\Delta Hep}$ mice and *Gsk3β* $^{fl/fl}$ mice. Scale bars: 100 μm (IHC) and 50 μm (IF). (*B*) Quantification of CYP2F2 positive area from IHC images. Positive area percentage was normalized to the number of PVs in the visual field quantified. Bar graphs represent the mean ± SD, * $P < .05$, **** $P < .0001$, ns, nonsignificant (1-way ANOVA with Bonferroni's multiple comparison).

mitochondria contact to explore the potential metabolic interactions between these organelles. We stained PMHs with MitoTracker and LipidTox dyes. Mitochondrial and LD staining revealed distinct mitochondrial morphology and LD contact between FFC-fed *Gsk3β*$^{\Delta Hep}$ and *Gsk3β*$^{fl/fl}$ PMH. In *Gsk3β*$^{fl/fl}$ PMHs, mitochondria appeared round, with an increased distance between mitochondria and LDs. In contrast, *Gsk3β*$^{\Delta Hep}$ PMH exhibited more elongated mitochondria with a shorter distance between the mitochondria and LDs (Figure 9*C, D*). Increased LD-mitochondria contact observed in *Gsk3β*$^{\Delta Hep}$ PMHs was further supported by increased perilipin 5 (*Plin5)* mRNA expression in the FFC-fed *Gsk3β*$^{\Delta Hep}$ vs *Gsk3β*$^{fl/fl}$ mice (Figure 9*E*). Plin5 is a LD membrane protein that facilitates LD-mitochondrial anchoring.[37] To further support our findings, we transfected AML12 cells with LD- and mitochondria-targeted split-FAST fragment (SPLICS FAST-LDh-MT-P2A) reporters to assess short-range LD-mitochondria contact sites. Treatment with PA reduced the SPLICs intensity, which was augmented by the GSK3 inhibitor (LY)

(Figure 9*F*). To examine changes in LD-mitochondria interactions, we acquired time-lapse images from AML12 cells treated with PA ± LY (Supplementary Videos 1 and 2) and performed distance analysis using the ImageJ program. Our quantitative data confirmed the increase in the number of LD-mitochondria interactions and contact surface area in hepatocytes under lipotoxic conditions treated with the GSK3 inhibitor LY (Figure 9*G*). Furthermore, time-lapse images showed that LDs dispersed among mitochondria with LY treatment, whereas they aggregated and fused into

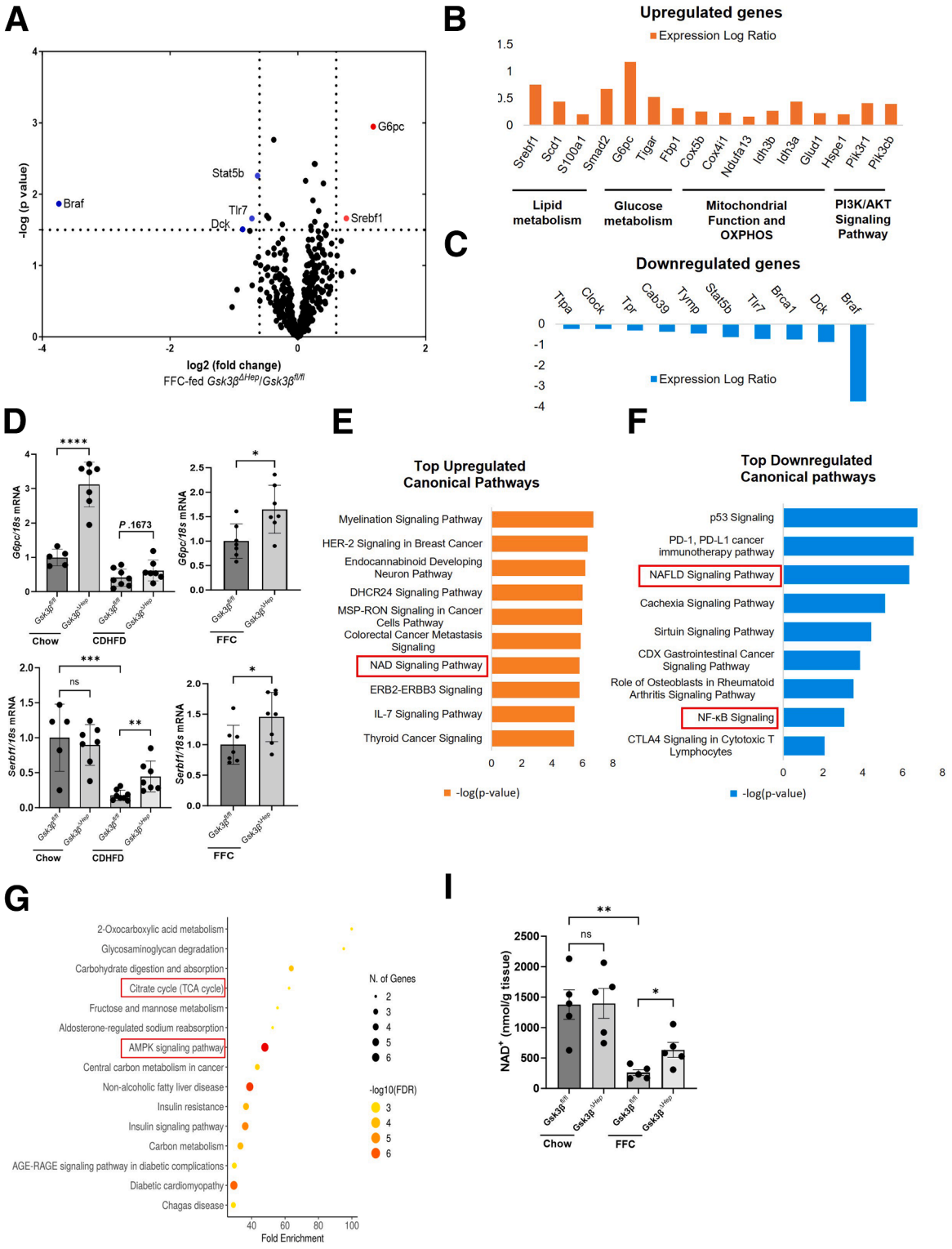

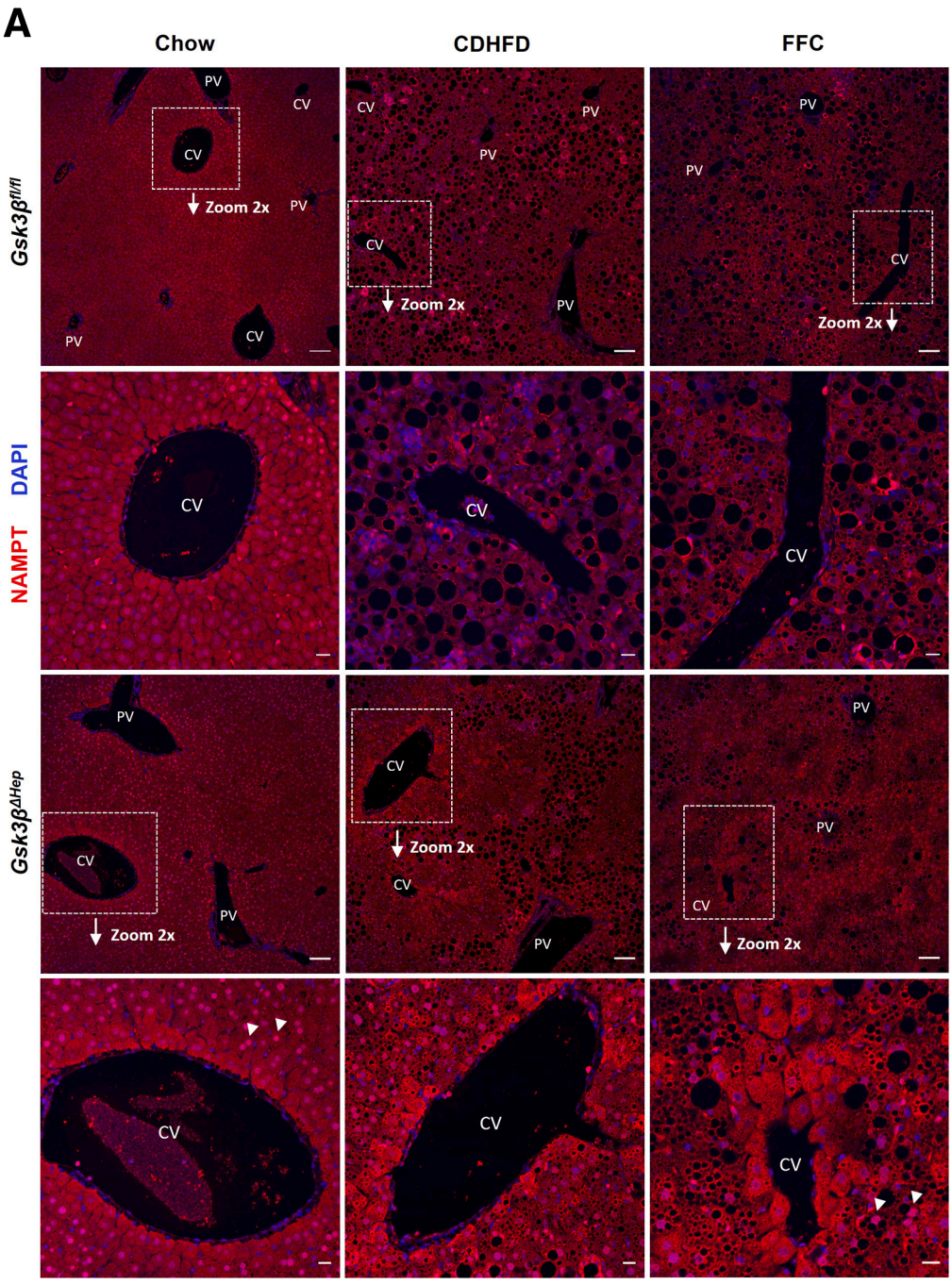

Figure 6. Immunofluorescence detection of pericentral Nampt restoration in *Gsk3β*$^{\Delta Hep}$ mice with diet induced MASH. (*A*) Representative immunofluorescence images of NAMPT in liver sections from CDHFD- and FFC-fed *Gsk3β*$^{\Delta Hep}$ and *Gsk3β*$^{fl/fl}$ mice, with associated zoomed-in images. *Arrowheads* indicate nuclear staining. Scale bars: 100 μm, 20 μm.

Figure 5. (***See previous page***). **Liver metabolic gene expression profile in *Gsk3β*$^{\Delta Hep}$ mice with FFC diet-induced MASH.** (*A*) Volcano plot showing differentially expressed genes ($P < .05$) in FFC-fed *Gsk3β*$^{\Delta Hep}$ mice versus *Gsk3β* $^{fl/fl}$ mice using the NanoString nCounter Metabolic Panel on liver tissue RNA. The X- and Y-axes represent the log2 fold-change (log_2FC) and log (*P* value) of the genes, respectively. *Red and blue circles* indicate the upregulated and downregulated genes, respectively, in FFC-fed *Gsk3β*$^{\Delta Hep}$ mice vs *Gsk3β* $^{fl/fl}$ mice (n = 3 per group). (*B*) Top upregulated genes and (*C*) downregulated genes ($P < .05$) in FFC-fed *Gsk3β*$^{\Delta Hep}$ versus *Gsk3β* $^{fl/fl}$ mice in the NanoString nCounter Metabolic Panel. (*D*) qPCR validation results of *G6pc* and *Srebf1,* significantly upregulated genes in the NanoString Metabolic Panel. (*E*) IPA analysis of NanoString Metabolic Panel data showing top upregulated and (*F*) downregulated canonical pathways. (*G*) ShinyGO analysis of NanoString Metabolic Panel data showing the most enriched pathways. (*I*) Liver NAD content in chow- and FFC-fed *Gsk3β*$^{\Delta Hep}$ and *Gsk3β*$^{fl/fl}$ mice (n = 5 per group). Bar graphs represent the mean ± SD; * $P < .05$, ** $P < .01$, *** $P < .001$, **** $P < .0001$, ns, nonsignificant (1-way ANOVA with Bonferroni's multiple comparison and unpaired *t*-test).

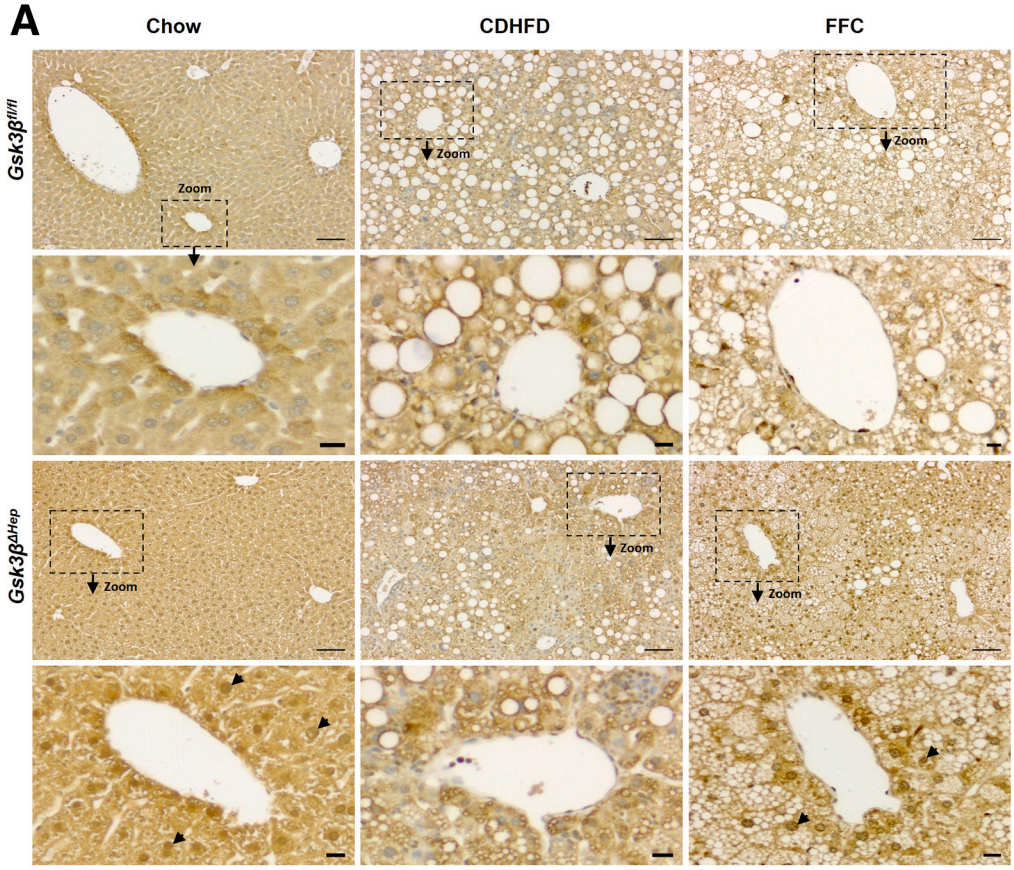

Figure 7. Immunohistochemistry (IHC) detection of pericentral Nampt restoration in *Gsk3β*$^{\Delta Hep}$ mice with diet induced MASH. (*A*) Representative IHC images of NAMPT in liver sections from CDHFD and FFC-fed *Gsk3β*$^{\Delta Hep}$ mice and *Gsk3β*$^{fl/fl}$ mice, with associated zoomed-in images. *Arrowheads* indicate nuclear staining. Scale bars: 100 μm, 20 μm.

larger LDs with PA treatment alone (Supplementary Videos 1 and 2). Taken together, these data indicate that *Gsk3β* deletion in hepatocytes enhances mitochondrial bioenergetics and hepatocyte respiratory capacity in MASH, likely by augmenting LD-mitochondria contact. We next explored how this biochemical alteration translates into physiological benefits in our *Gsk3β*$^{\Delta Hep}$ mouse model, particularly focusing on the attenuation of MASH.

Hepatocyte Gsk3β Deletion Reduces Liver Injury and Ferroptosis in Murine MASH

To assess the impact of *Gsk3β*$^{\Delta Hep}$ on liver injury in mice with diet-induced MASH, we measured serum alanine aminotransferase (ALT) levels and identified a significant reduction in ALT levels in CDHFD-fed *Gsk3β*$^{\Delta Hep}$ mice compared with *Gsk3β*$^{fl/fl}$ mice (Figure 10*A*). Comparable results were observed in the FFC-fed mice (Figure 11*A*). We further examined the role of hepatocyte GSK3B in diet-induced hepatocyte death using the ApopTag assay and identified a significant decrease in cell death in CDHFD-fed *Gsk3β*$^{\Delta Hep}$ mice compared with *Gsk3β*$^{fl/fl}$ mice (Figure 10*B*). Similarly, FFC-fed *Gsk3β*$^{\Delta Hep}$ mice displayed significantly reduced ApopTag staining compared with FFC-fed *Gsk3β*$^{fl/fl}$ mice (Figure 11*B*). To examine whether ferroptosis reduction is the underlying mechanism of attenuated hepatocyte injury in *Gsk3β*$^{\Delta Hep}$ mice fed a MASH-inducing diet, we assessed the expression levels of key ferroptosis markers in the liver tissues of mice from the different experimental groups and identified downregulation in the mRNA levels of acyl-CoA synthetase long-chain family member 4 (*Acsl4*), prostaglandin-endoperoxide synthase 2 (*Ptgs2*), and ferritin heavy polypeptide 1 (*Fth1*), whereas the levels of ferroptosis suppressor protein 1 (*Fsp1*) mRNA expression were upregulated in CDHFD-fed *Gsk3β*$^{\Delta Hep}$ mice compared with controls (Figure 10*C*). To determine whether Gsk3*β* deletion in hepatocytes decreased MASH-induced oxidized phospholipid (OxPL) accumulation and ferroptosis, we evaluated the presence of OxPLs in liver tissues using 4-hydroxy-2-nonenal (4-HNE) and oxidized 1-palmitoyl-2-arachidonoyl-sn-glycero-3-phosphorylcholine (oxPAPC) staining, which showed decreased OxPLs in CDHFD-fed *Gsk3β*$^{\Delta Hep}$ versus *Gsk3β*$^{fl/fl}$ mice (Figure 10*B*). Likewise, the hepatic expression of transferrin receptor 1 (TFRC), a membrane protein crucial for iron uptake, was reduced in CDHFD-fed *Gsk3β*$^{\Delta Hep}$ mice (Figure 10*B*). These findings were also recapitulated in FFC-fed mice (Figure 11*B*). Furthermore, the measurement of liver malondialdehyde (MDA), a biomarker for oxidative stress and lipid peroxidation in cells and tissues, confirmed that GSK3*β* deletion ameliorated ferroptotic stress in *Gsk3β*$^{\Delta Hep}$ vs *Gsk3β*$^{fl/fl}$ mice on the MASH-inducing diet (Figures 10*D*, 11*C*), with a stronger ferroptotic signature induced by the CDHFD diet than in the FFC diet. 4-HNE is highly reactive and binds to biomolecules including lipids, proteins, and nucleic acids. HNE-protein adducts are the most abundant forms of HNE and have been implicated in age-related diseases and increased oxidative stress.[38] Therefore, HNE-

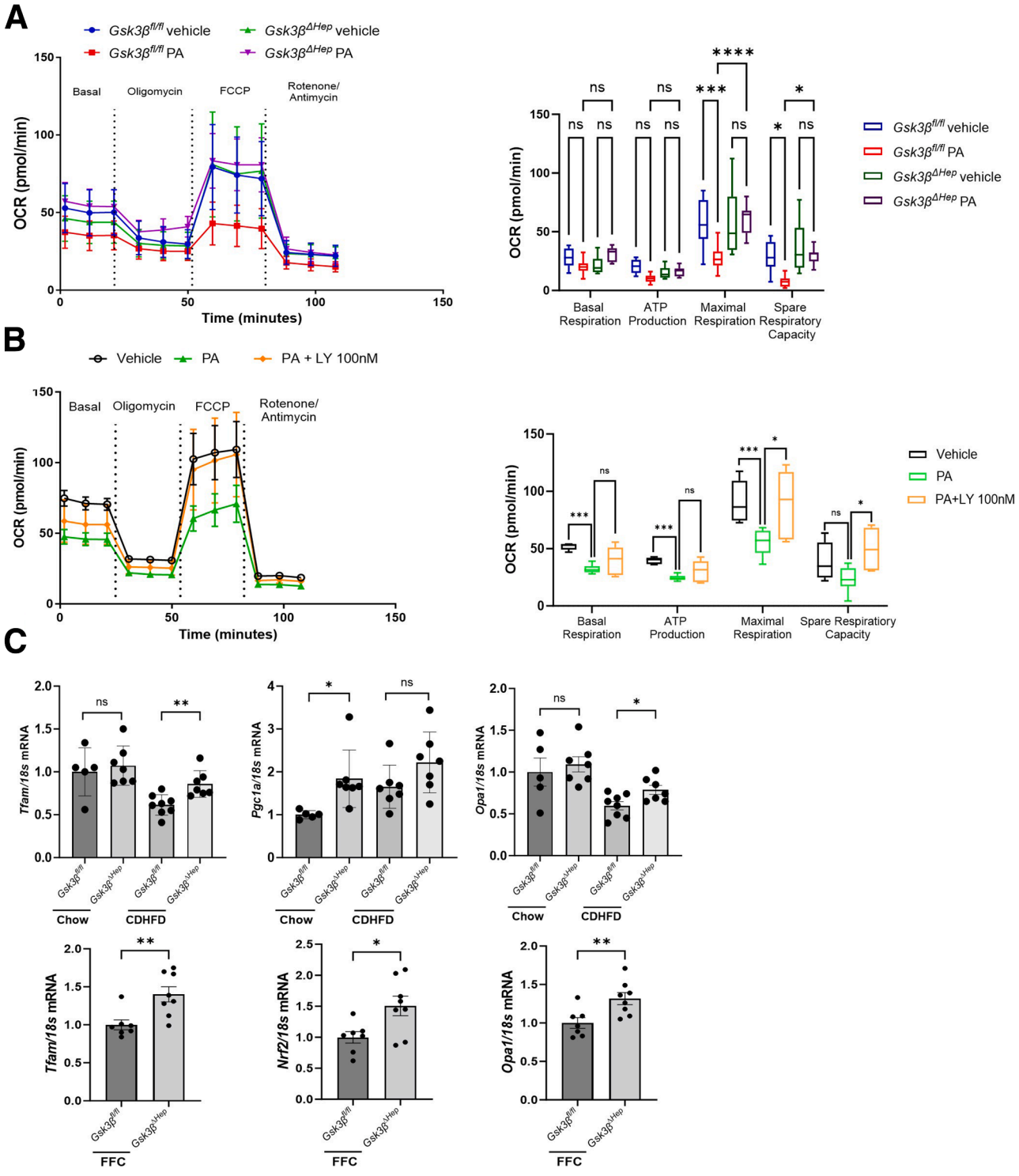

Figure 8. GSK3β inhibition enhances mitochondrial bioenergetics during lipotoxicity and MASH. (*A*) OCR of PMH cells from *Gsk3β*$^{\Delta Hep}$ vs *Gsk3β* $^{fl/fl}$ mice measured by the Seahorse mitochondrial respiratory assay at baseline and in response to oligomycin, FCCP, and rotenone plus antimycin A. PMH cells were treated with 500 μM PA for 4 hours before the assay. Basal respiration, ATP production, proton leakage, maximal respiration, and spare capacity were analyzed. (n = 6) (*B*) OCR of AML12 cells measured by the Seahorse mitochondrial respiratory assay at baseline and in response to oligomycin, FCCP, and rotenone plus antimycin A. Cells were pretreated for 2 hours with 100 nM LY, followed by 4hr treatment with 500 μM PA ± 100 nM LY before the assay (n = 6). (*C*) mRNA expression of mitochondrial transcription factor A (*Tfam*), peroxisome proliferator-activated receptor gamma coactivator 1-alpha (*Pgc1a*), nuclear factor erythroid 2-related factor 2 (*Nrf2*), and optic atrophy 1 (*Opa1*) (n = 5–8 per group). Bar graphs represent the mean ± SD; * $P < .05$, ** $P < .01$, *** $P < .001$, **** $P < .0001$, ns, nonsignificant (1-way ANOVA with Bonferroni's multiple comparison and unpaired *t*-test).

protein adducts are plausible markers and mediators of oxidative stress and lipid peroxidation and can be detected using a Western blot-based approach.[39] Our data indicate that HNE-protein adducts were lower in liver tissues of CDHFD-fed $Gsk3\beta^{\Delta Hep}$ mice than in $Gsk3\beta^{fl/fl}$ mice, further supporting the lower levels of lipid peroxidation

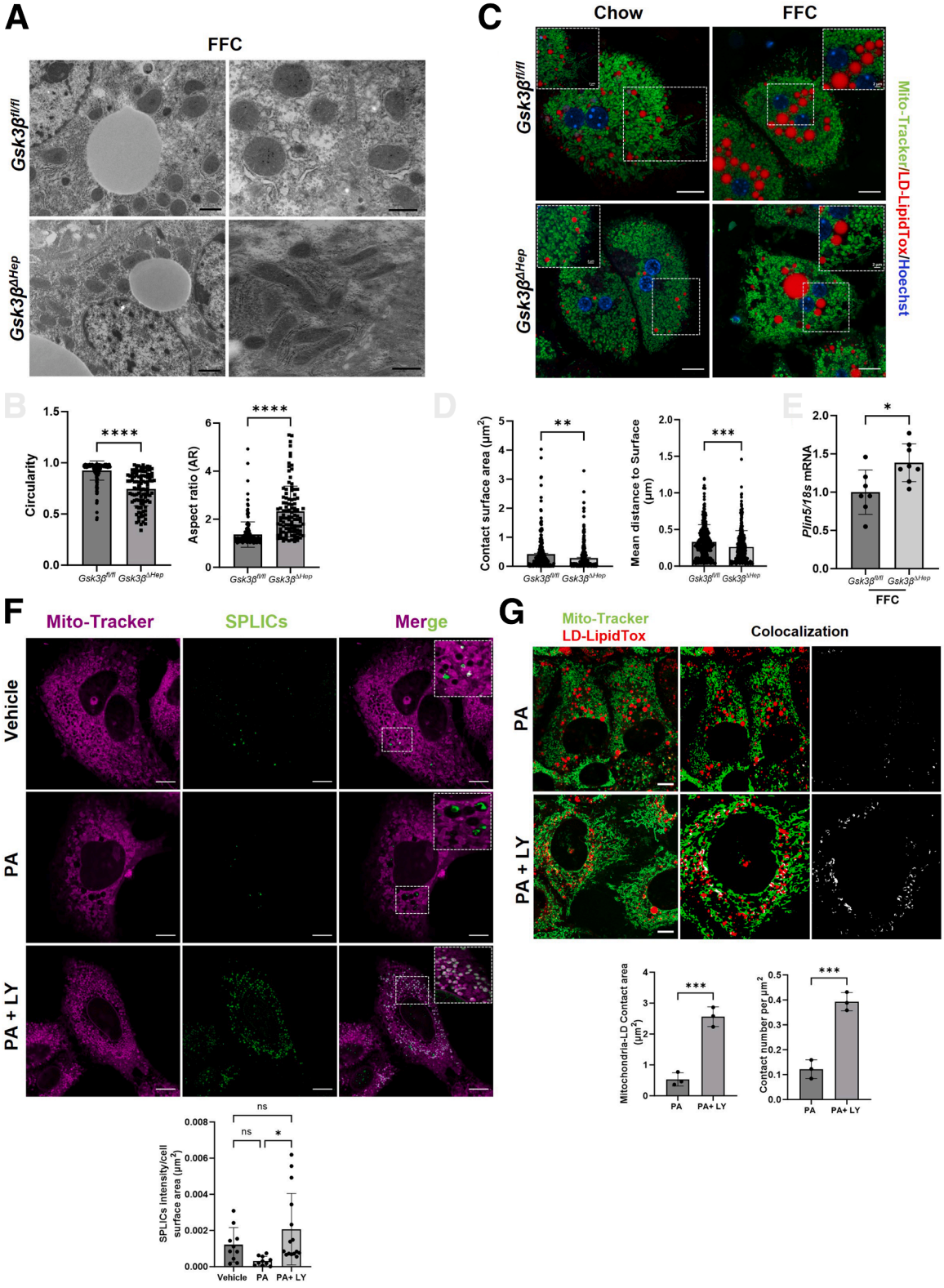

(Figure 11*D*). To assess whether the reduced ferroptotic injury observed in the *Gsk3β*$^{\Delta Hep}$ mice could be recapitulated pharmacologically, liver samples were collected from mice fed a CDHFD and treated with the GSK3β inhibitor Elraglusib or 9-ING-41(ING), followed by analysis of ferroptosis markers. Consistent with the *Gsk3β*$^{\Delta Hep}$ mice, CDHFD-fed mice treated with the GSK3 inhibitor ING showed reduction in the expression of ferroptosis markers *Acsl4* and *Ptgs2* (Figure 12*A*). Additionally, immunohistochemistry staining of liver tissues from FFC-fed mice treated with the GSK3β inhibitor LY showed lower levels of the ferroptosis markers 4-HNE, oxPAPC, and TFRC (Figure 12*B*). Overall, pharmacological inhibition of GSK3β elicited a comparable outcome, further substantiating the mechanistic role of GSK3β in ferroptotic injury in MASH. To assure the human relevance of GSK3β signaling and ferroptosis in MASH, we previously showed increased GSK3β activating phosphorylation in human liver samples of patients with MASH compared with patients with steatosis and normal liver.[23] In the current study, we examined the presence of ferroptotic damage in the liver tissues of patients with MASH and identified increased ferroptosis markers in MASH liver samples compared with those in simple steatosis and control samples, including increased 4-HNE and hyperoxidized peroxiredoxin 3 (PRDX3) levels[40] (Figure 12*C*). Taken together, these observations support the notion that ferroptotic injury is prevalent in human and murine MASH and that GSK3β inhibition attenuates ferroptotic injury in murine MASH.

GSK3β Inhibition Modulates Lipotoxicity-induced Ferroptosis in Hepatocytes by Regulating FSP1 Localization

To investigate whether PA induces ferroptosis in hepatocytes, we assessed the viability of AML12 cells treated with PA ± Fer-1, a potent ferroptosis inhibitor. Notably, Fer-1 rescued PA-induced reduction in hepatocyte viability, suggesting a key role for ferroptosis in lipotoxicity-induced cell death (Figure 13*A*). Given that glutathione peroxidase 4 (GPX4) pathway is the main protective pathway against ferroptosis in mammalian cells, we examined GPX4 protein levels in AML12 cells treated with PA and observed no significant changes (Figure 13*B*). Likewise, the mRNA and protein levels of *Gpx4* were not significantly different between *Gsk3β*$^{\Delta Hep}$ and *Gsk3β*$^{fl/fl}$ mice fed MASH-inducing diets (Figure 13 *C–E*), suggesting that GSK3β may modulate ferroptosis independently of GPX4.

FSP1 expression correlates with ferroptosis resistance in cells, and its activity is modulated by regulating its enzymatic activity and subcellular localization.[41,42] In addition, emerging data suggest that FSP1-mediated LD quality control prevents neutral lipid peroxidation and ferroptosis.[43] To assess alterations in FSP1 dynamics and subcellular localization, we transfected the human hepatocyte cell line Huh7 with hFSP1–EGFP–Strep plasmid. FSP1 was localized to the LDs monolayer under basal conditions and became more prominent in the presence of the GSK3 inhibitor LY (Figure 14*A, B*). Our data are consistent with a previous report on the subcellular localization of FSP1.[41] Treatment with icFSP1, a potent FSP1 inhibitor, triggered FSP1 phase separation and condensate formation in Huh7 cells. Cells treated with PA formed condensates similar to icFSP1-treated cells, whereas LY treatment of PA-treated cells reduced FSP1 phase separation without altering FSP1 localization to the LDs monolayer (Figure 14*A*). Although FSP1 did not localize to the mitochondrial membrane, treatment with LY increased mitochondrial contact with LD-localized FSP1 (Figure 14*B*). Taken together, these data suggest that GSK3β inhibition modulates lipotoxicity-induced hepatocyte ferroptosis independently of the GPX4 axis, likely by altering FSP1 subcellular localization dynamics.

Hepatocyte Gsk3β Deletion Protects Against Liver Inflammation in Murine MASH

Histological analysis of hematoxylin and eosin (H&E)-stained liver sections indicated reduced lobular inflammation and hepatocyte ballooning scores in *Gsk3β*$^{\Delta Hep}$ mice compared with *Gsk3β*$^{fl/fl}$ mice on the CDHFD (Figure 15*A, B*) and FFC (Figure 16*A*) diets. Likewise, immunostaining for F4/80, a macrophage marker (Figure 15*C*), and myeloperoxidase (MPO), a marker of neutrophil infiltration (Figure 15*D*), was significantly reduced in CDHFD-fed *Gsk3β*$^{\Delta Hep}$ mice compared with *Gsk3β*$^{fl/fl}$ mice fed the same diet. Similarly, FFC-fed *Gsk3β*$^{\Delta Hep}$ mice showed reduced myeloid cell infiltration (Figure 16*B, C*). Given its role in MASH-associated hepatic fibrosis,[44] we examined the levels of neutrophil extracellular traps (NETs) and

Figure 9. (***See previous page***). **GSK3β inhibition in hepatocytes ameliorates mitochondrial morphology and increases LD-mitochondria contact under toxic lipid treatment and in murine MASH.** (*A*) EM images of mitochondrial morphology. Scale bars: 1 μm (*left*), 600 nm (*right*). (*B*) Quantification of circularity and aspect ratio. Circularity (a measure of how close the shape of the mitochondrion is to a perfect circle) ranges from 1 (perfect circle) to 0 (more elongated or irregular shapes). The AR (ratio of the major to minor axis of the mitochondrion) measures mitochondrial elongation, with higher values indicating more elongated mitochondria (n = 3 per group). (*C*) Primary mouse hepatocytes were stained with MitoTracker (*green*) to visualize the mitochondria and LipidTox (*red*) to label LDs. Nuclei were counterstained with DAPI (*blue*) (n = 1 per group). Scale bar: 10 μm. (*D*) Quantification of LD-mitochondrial contacts. (*E*) Perilipin 5 (*Plin5*) mRNA expression (n = 7–8 per group). (*F*) Representative images of LD- and mitochondria-targeted split-FAST fragments for short-range LD-MT contact sites (SPLICs) in AML12 cells treated with 500 μM PA ± 100 nM LY. Cells were stained with MitoTracker (DsRed) to visualize the mitochondria (*top panel*). Quantification of SPLICs intensity (*bottom panel*). Scale bar: 10 μm. (*G*) Quantification of the LD-mitochondrial contact site area and number in AML12 cells treated with 500 μM PA ± 20 nM LY. Cells were stained with MitoTracker (*green*) to visualize the mitochondria and LipidTox (*red*) to label LDs (n = 3 per group). Scale bar: 10 μm. Bar graphs represent mean ± SD; * $P < .05$, ** $P < .01$, *** $P < .001$, **** $P < .0001$, ns, nonsignificant (unpaired *t*-test).

identified reduced citrullinated histone 3 (CitH3) staining in CDHFD-fed *Gsk3β*$^{\Delta Hep}$ mice compared with that in *Gsk3β*$^{fl/fl}$ mice (Figure 15*D*). Additionally, CDHFD-fed *Gsk3β*$^{\Delta Hep}$ mice showed reduced mRNA expression of proinflammatory monocytes and chemokines, including C-C motif chemokine ligand 2 (*Ccl2*), C-C chemokine receptor type 2 (*Ccr2*), and C-X-C motif chemokine ligand 2 (*Cxcl2*) (Figure 15*E*). These markers also decreased in FFC-fed

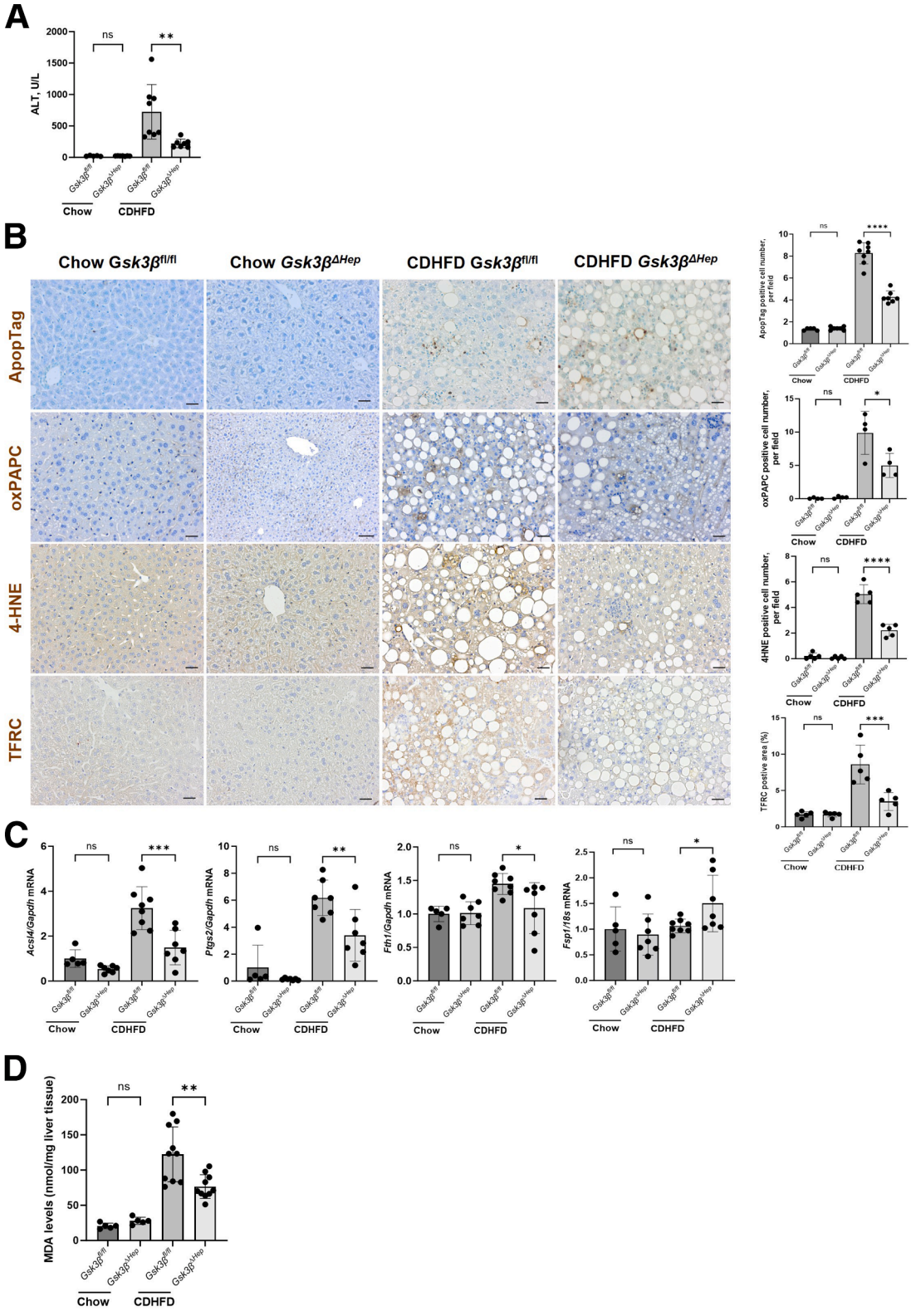

mice (Figure 16*D*). Thus, GSK3β deletion in hepatocytes attenuates hepatic inflammation in murine MASH mainly by reducing hepatic myeloid cell infiltration.

Because GSK3β plays a significant role in regulating mitochondrial membrane potential and mitochondrial permeability transition pore (mPTP) dynamics,[22,45] we assessed whether *Gsk3β* deletion in hepatocytes alters the release of mitochondrial DNA (mtDNA), a DAMP that contributes to the sterile proinflammatory response in MASH via TLR9 activation.[46] CDHFD-fed $Gsk3\beta^{\Delta Hep}$ mice showed a marked decrease in serum mtDNA levels compared with $Gsk3\beta^{fl/fl}$ mice, indicating a protective effect against mitochondrial oxidative stress and damage (Figure 15*F*). Likewise, PA-induced mtDNA release in the conditioned media from $Gsk3\beta^{\Delta Hep}$ PMHs was significantly reduced compared with that in $Gsk3\beta^{fl/fl}$ PMHs (Figure 15*G*). Taken together, these data indicate that *Gsk3β* deletion in hepatocytes alleviates mtDNA release from hepatocytes and associated myeloid cell infiltration and NETosis formation.

Hepatocyte Gsk3β Deletion Attenuates Liver Fibrosis

Next, we assessed the effect of hepatocyte *Gsk3β* deletion on liver fibrosis. $Gsk3\beta^{\Delta Hep}$ mice showed a significant reduction in Sirius Red staining (Figure 17*A*) and alpha-smooth muscle actin (αSMA) immunostaining (Figure 17*B*) compared with $Gsk3\beta^{fl/fl}$ mice fed the CDHFD diet. These findings were supported by the reduction in *Col1a1* mRNA expression in $Gsk3\beta^{\Delta Hep}$ mice (Figure 17*C*). In comparison, FFC-fed $Gsk3\beta^{\Delta Hep}$ mice displayed a significant reduction in the fibrosis signature (Figure 18*A*–*B*), further validating our findings in CDHFD-fed mice.

To further investigate the underlying mechanism of attenuated fibrosis in $Gsk3\beta^{\Delta Hep}$ mice fed the MASH-inducing diet, we applied the fibrosis gene expression panel from NanoString on RNA isolated from the liver tissue from the different experimental groups of the CDHFD feeding study and identified 78 differentially expressed genes (Figure 17*D*). Gene expression analysis revealed the downregulation of multiple profibrogenic genes, including thrombospondin-I (*Thbs1*), lysyl oxidase (*Lox*), C/EBP homologous protein (*Chop*), and plasminogen activator inhibitor-1 (Serpine1) (Figure 17*D*–*E*). Furthermore, IPA identified 98 canonical pathways that were differentially regulated in $Gsk3\beta^{\Delta Hep}$ mice on the CDHFD diet compared with $Gsk3\beta^{fl/fl}$ (z-score $> \pm 2.0$ and $P < .05$), including hepatic fibrosis and integrin cell surface interactions, highlighting the pathogenic role of hepatocyte GSK3β in driving liver fibrosis in MASH (Figure 17*F*).

Discussion

This study provides mechanistic insights into the role of hepatocyte GSK3β in lipotoxicity-induced liver injury, inflammation, and fibrosis in MASH. Herein, our data indicate that: (1) in hepatocytes under lipotoxic stress, GSK3β pharmacological or genetic inhibition improves mitochondrial bioenergetics and morphology, increases the abundance of LD-associated mitochondria, elevates NAD^+ levels, restores cytosolic pericentral and nuclear Nampt expression, and reduces ferroptosis, likely via an FSP1-dependant mechanism; and (2) hepatocyte-specific deletion of *Gsk3β* in 2 different mouse models of MASH reduces liver injury, ferroptosis markers, and circulating mitochondrial DNA release, thereby ameliorating myeloid cell hepatic infiltration and liver inflammation and fibrosis in MASH.

The pathogenesis of MASH involves complex interactions between metabolic and inflammatory pathways, with hepatocyte cell death being a central feature. Therefore, identifying the molecular mediators involved in the activation of cell death pathways in MASH is crucial for advancing our understanding of disease pathogenesis and developing mechanism-based therapeutic strategies. Ferroptosis is driven by iron-dependent lipid peroxidation and has been implicated in the pathogenesis of MASLD.[47] The availability and subcellular localization of lipids, ROS, and iron homeostasis influence ferroptosis and the cellular response to ferroptotic stress, highlighting the complexity of this regulated cell death mechanism. To the best of our knowledge, this is the first study to elucidate the pathogenic role of GSK3β in lipotoxicity-induced ferroptosis in MASH. The observed reduction in ferroptosis markers in $Gsk3\beta^{\Delta Hep}$ mice with MASH directly correlated with our in vitro findings of improved mitochondrial bioenergetics, suggesting a mechanistic pathway in which GSK3β inhibition directly and indirectly mitigates ferroptosis. Notably, pharmacological and genetic inhibition of GSK3β in hepatocytes rescues mitochondrial respiration and enhances mitochondrial bioenergetics under lipotoxic conditions. The role of mitochondria in regulating ferroptosis sensitivity is context-dependent.[48] Some studies suggest that mitochondria play a role in cysteine deprivation-induced ferroptosis but not in GPX4 inhibition-induced ferroptosis.[49] Conversely, mitochondria have also been identified as inhibitors of ferroptosis via β-oxidation regulation,

Figure 10. (*See previous page*). Hepatocyte-specific *Gsk3β* deletion attenuates ferroptosis and liver injury in CDHFD-induced murine MASH. (*A*) Serum levels of ALT (n = 5–8 per group). (*B*) Immunohistochemical staining of ApopTag Peroxidase, oxPAPC, 4-HNE, and TFRC in liver sections from CDHFD-fed $Gsk3\beta^{\Delta Hep}$ and $Gsk3\beta^{fl/fl}$ mice (*left panels*). The ApopTag-positive area was quantified in 5 random 20× microscopic fields and averaged for each animal (right panel). oxPAPC and 4-HNE-positive cells were quantified in 5 random 20× microscopic fields and averaged for each animal (*right panels*). TFRC-positive area was quantified in 5 random 20× microscopic fields and averaged for each animal (*right panel*) (n = 4–8 per group). (*C*) mRNA expression of acyl-CoA synthetase long-chain family member 4 (*Acsl4*), prostaglandin-endoperoxide synthase 2 (*Ptgs2*), ferritin heavy polypeptide 1 (*Fth1*), and ferroptosis suppressor protein 1 (*Fsp1*) (n = 5–8 per group). (*D*) Quantification of hepatic MDA levels in CDHFD-fed $Gsk3\beta^{fl/fl}$ and $Gsk3\beta^{\Delta Hep}$ mice (n = 5–10 per group). Bar graphs represent the mean ± SD; * $P < .05$, ** $P < .01$, *** $P < .001$, **** $P < .0001$, ns, nonsignificant (1-way ANOVA with Bonferroni's multiple comparison). Scale bar: 20 μm (*B*).

detoxification of lipid peroxides, and modulation of iron metabolism.[50] The electron transport chain enhances ferroptosis resistance by maintaining the activity of dihydroorotate dehydrogenase (DHODH) and glycerol-3-phosphate dehydrogenase 2 (GPD2), which generate reduced mitochondrial Coenzyme Q (CoQ).[51,52]

In addition to their role in energy storage, LDs function as hubs of cellular signaling and buffers by sequestering

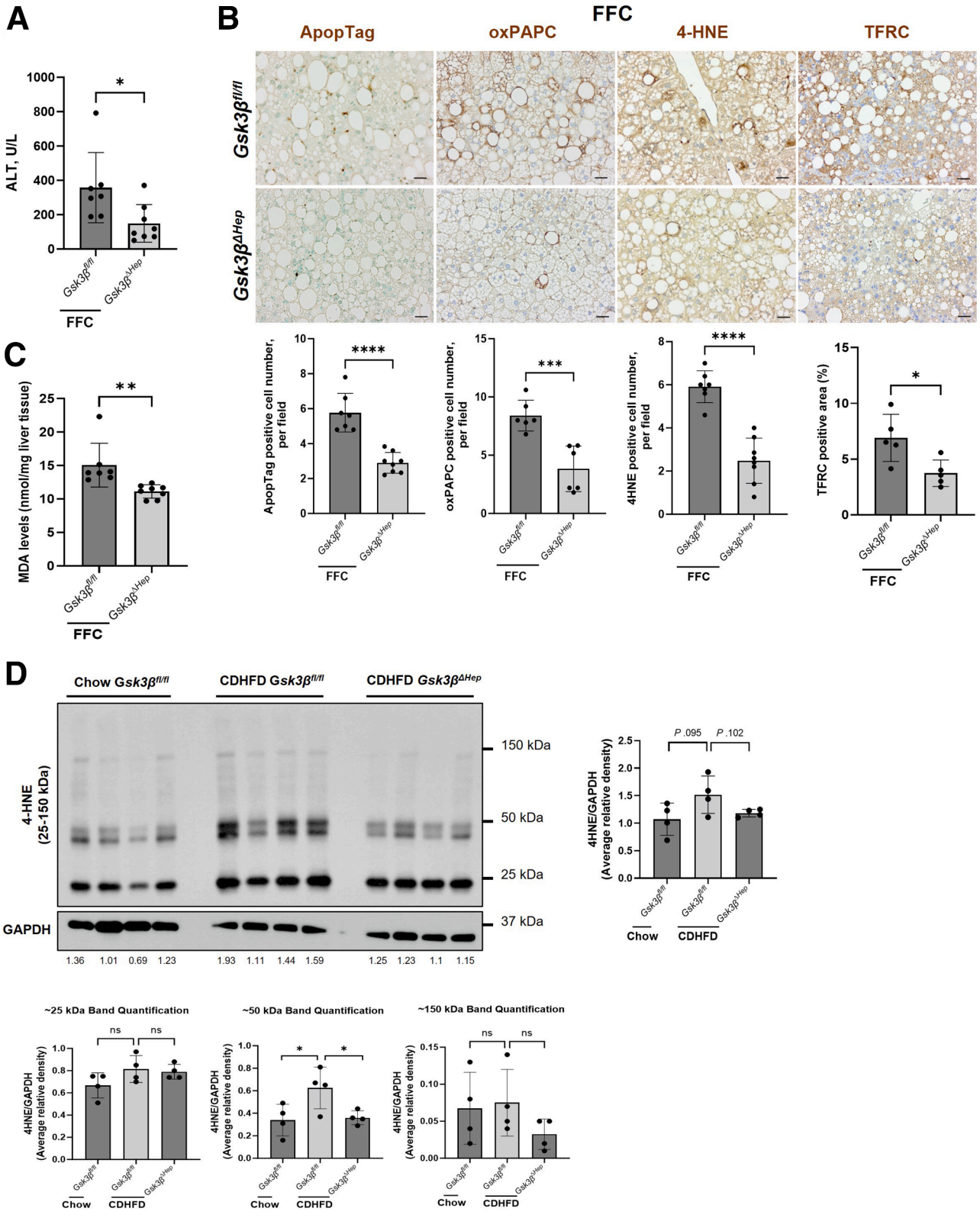

FAs under lipotoxic conditions. In accordance with recent research,[43] we demonstrate that FSP1 localizes to LDs under lipotoxic conditions in the presence of GSK3 inhibition. LD-localized FSP1 acts as a quality control pathway that maintains the integrity of neutral lipids and prevents lipid peroxidation. Importantly, our results indicate that GSK3β inhibition increases LD-mitochondrial contact, which plays a vital role in lipid trafficking, mitochondrial protection during lipotoxicity, energy production, and metabolic regulation based on energy demands.[12] Furthermore, we identified *Srebf1* upregulation in the *Gsk3*$\beta^{\Delta Hep}$ mice fed the MASH-inducing diet. *Srebf1* induces the expression of SCD1 that catalyzes the synthesis of long-chain mono-saturated fatty acids (MUFAs) which in turn reduce the levels of oxidizable PUFAs, thereby decreasing the sensitivity of plasma membrane lipids to oxidation and ferroptosis.[53] MUFAs produced by SCD1 are crucial for maintaining the fluidity of the mitochondrial membrane, which is essential for optimal mitochondrial function, including electron transport chain efficiency and ATP production. Conversely, SCD1 deficiency is associated with increased membrane lipid saturation, leading to decreased mitochondrial membrane fluidity, which may impair mitochondrial function by affecting the dynamics of membrane-associated processes, such as the formation of contact sites with other organelles. Thus, deletion of *Gsk3*β in hepatocytes may confer resistance to ferroptosis by upregulating the SREBF1-SCD1 axis. Collectively, these findings support the notion that GSK3β inhibition increases the metabolic resilience and ferroptosis resistance of hepatocytes under lipotoxic conditions.

Ferroptosis results in the release of DAMPs, cytokines, and chemokines, which recruit and activate myeloid cells.[54,55] The release of mtDNA from injured hepatocytes triggers a potent inflammatory response, exacerbates hepatocellular damage, and promotes fibrosis.[56] We demonstrated that mtDNA, a vital component of mitochondria-derived DAMPs, was reduced in the serum of *Gsk3*$\beta^{\Delta Hep}$ mice with MASH and in the conditioned medium of PA-treated *Gsk3*$\beta^{\Delta Hep}$ PMH. These findings indicate that GSK3β regulates mtDNA release from hepatocytes, likely by reducing mitochondrial oxidative stress and preventing the opening of the mitochondrial permeability transition pore, which in turn reduces liver injury, inflammation, and fibrosis.

To contextualize our findings within the broader field, we propose that the modulation of ferroptosis and mitochondrial dysfunction by GSK3β in hepatocytes presents a novel therapeutic target for MASH. Future studies should explore the translational potential of GSK3β inhibitors in clinical settings.

Methods

Materials

The primary antibodies employed in the study include anti-α-SMA (ab124964) from Abcam, anti- glyceraldehyde-3-phosphate dehydrogenase (GAPDH) (MAB374) from Millipore Sigma, anti-MPO (#AF3667) from R&D systems, anti-nicotinamide phosphoribosyl transferase (NAMPT) (#A11776-1-AP) from Proteintech, anti-F4/80 (#70076S) from Cell Signaling Technology, anti-4-HNE antibody (MAB3249), and human/mouse/rat GPX4 (h/m/rGPX4) antibody (MAB5457) from R&D Systems, anti-oxidized phospholipid (oxPAPC) antibody (MABS2278) from Sigma-Aldrich (Merck KGaA), anti-TFRC antibody (ab214039) from Abcam, hyperoxidized peroxiredoxin-3 polyclonal ($SO_{2/3}$-PRDX3) antibody (#39806) from Cayman Chemical, GS antibody (#G2781) from Sigma-Aldrich, CYP2F2 (#sc-374540) antibody from Santa Cruz Biotechnology, vinculin (7F9) antibody (#sc-73614) from Santa Cruz, and Cit-Histone H3 (Arg2, Arg8, Arg17) polyclonal (#630-180) antibody from ThermoFisher. PA (P0500) was purchased from Sigma-Aldrich. LY (S7063) was purchased from Selleck Chemicals. Elraglusib (9-ING-41) was kindly provided by Acuate Therapeutics Inc.

Animals

All animal studies were approved and performed in accordance with the Institutional Animal Care and Use Committee (IACUC) at the Mayo Clinic. Male C57Bl/6J mice were purchased from the Jackson Laboratory. Hepatocyte-specific *Gsk3*β knockout (*Gsk3*$\beta^{\Delta Hep}$) mice were generated by crossing *Gsk3*$\beta^{fl/fl}$ mice with albumin-Cre mice. In *albCre* transgenic mice, Cre is driven by the serum *albumin* (*alb*) gene (exclusively expressed in hepatocytes and induced at differentiation) promoter and involves Cre-dependent excision of *lox*P-flanked (floxed) sequences in adult hepatocytes. Developmentally, recombination

Figure 11. (***See previous page***). **Hepatocyte-specific *Gsk3*β deletion attenuates liver injury and oxidized phospholipid accumulation in FFC-induced murine MASH.** (*A*) Serum levels of ALT (n = 7–8 per group). (*B*) Immunohistochemical staining of ApopTag Peroxidase, oxPAPC, 4-HNE, and TFRC in liver sections from FFC-fed *Gsk3*$\beta^{\Delta Hep}$ and *Gsk3*$\beta^{fl/fl}$ mice (*top panels*). The ApopTag-positive area was quantified in 5 random 10× microscopic fields and averaged for each animal (*bottom*) (n = 7–8 per group). oxPAPC-positive cells were quantified in 5 random 20× microscopic fields and averaged for each animal (*bottom*) (n = 6 per group). 4-HNE-positive cells were quantified in 5 random 20× microscopic fields and averaged for each animal (*bottom*) (n = 7–8 per group). TFRC-positive area was quantified in 5 random 20× microscopic fields and averaged for each animal (*bottom*) (n = 5 per group). (*C*) Quantification of hepatic MDA levels in FFC-fed *Gsk3*$\beta^{fl/fl}$ and *Gsk3*$\beta^{\Delta Hep}$ mice (n = 7–8 per group). (*D*) Representative Western blot images showing 4-HNE-modified proteins in CDHFD-fed *Gsk3*$\beta^{\Delta Hep}$ mice and *Gsk3*$\beta^{fl/fl}$ mice. The total protein bands of various molecular weights indicate the presence of 4-HNE adducts (*left panel*). Quantification of 4-HNE protein adducts was normalized to GAPDH (*right and bottom panels*). Bar graphs represent the mean ± SD; * $P < .05$, ** $P < .01$, *** $P < .001$, **** $P < .0001$, ns, nonsignificant (1-way ANOVA with Bonferroni's multiple comparison). Scale bar: 20 μm (*B*).

typically begins around embryonic day 14.5 (E14.5). This timing aligns with the developmental onset of *alb* gene expression in hepatoblasts, the precursor cells of hepatocytes.[57] Hence, unlike the global deletion of *Gsk3β* that results in embryonic lethality due to liver apoptosis, as shown by Hoeflich et al,[58] *Gsk3β* $^{\Delta Hep}$ are viable and

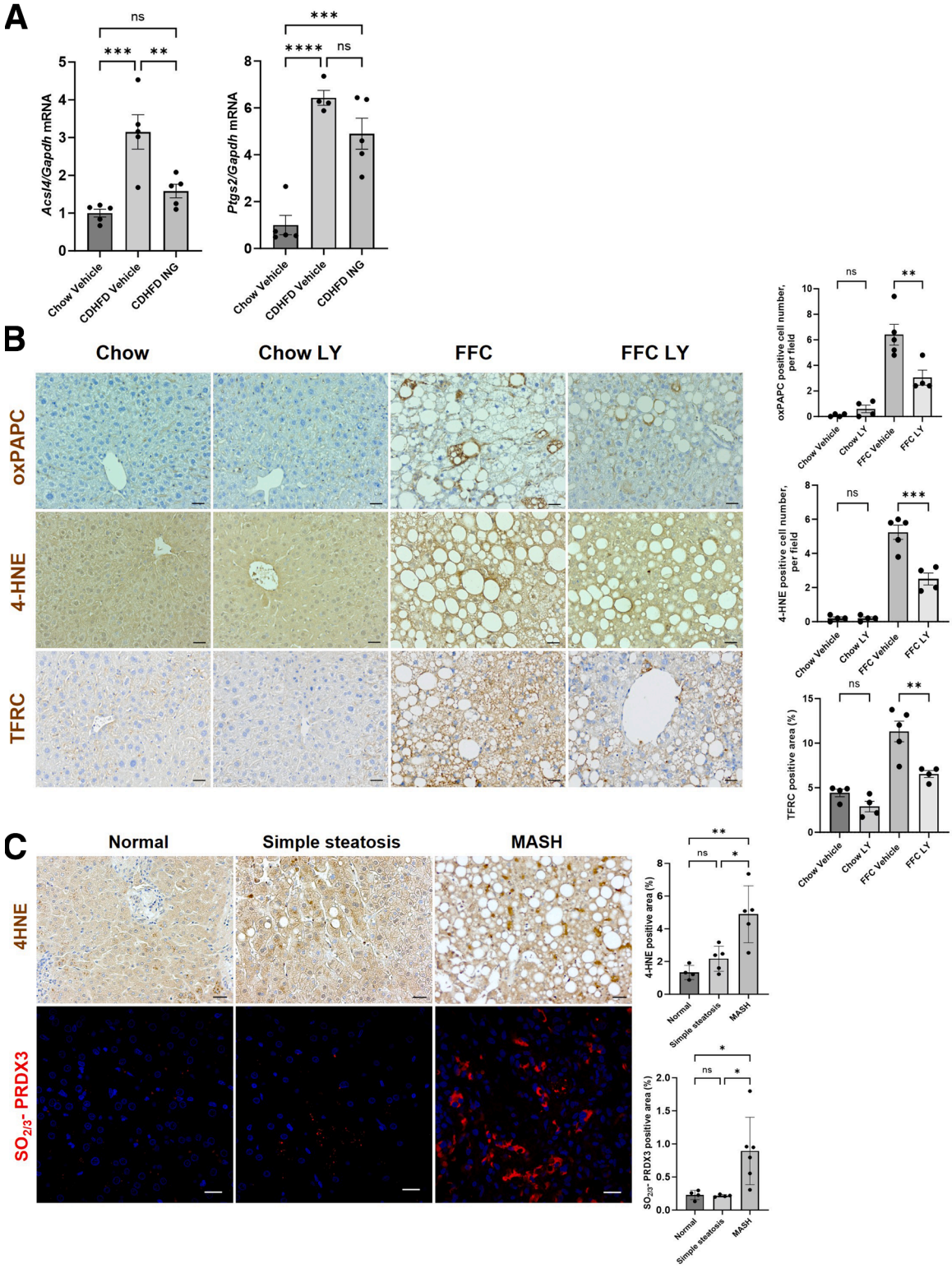

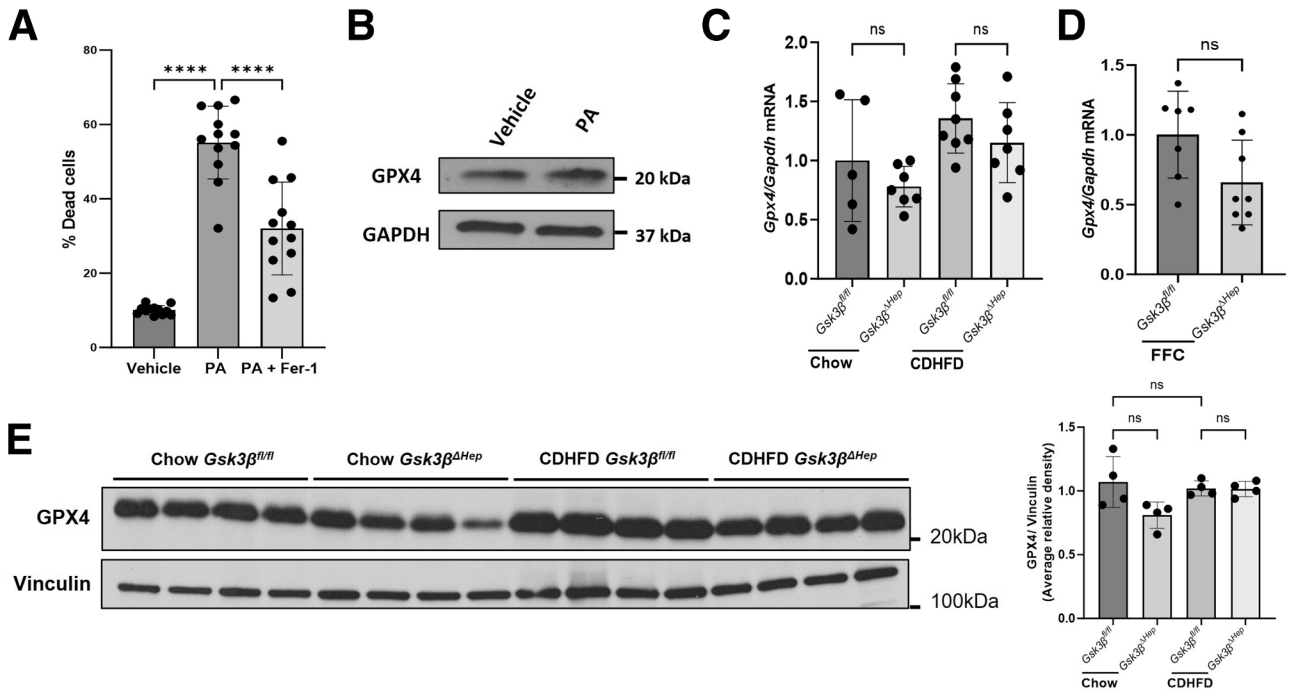

Figure 13. Lipotoxic stress induces hepatocyte ferroptosis. (*A*) AML12 cells were treated with 500 μM PA ± the ferroptosis inhibitor Fer-1, and cell viability was assessed after 16 hours using a Celigo Imaging Cytometer (n = 12). (*B*) Western blotting for GPX4 protein in AML12 cells treated with 500 μM PA for 2 hours. (*C*) mRNA expression of *Gpx4* in CDHFD-fed mice (n = 5–8 per group). (*D*) mRNA expression of *Gpx4* in FFC-fed mice (n = 7–8 per group). (*E*) Representative Western blot images showing GPX4 proteins in CDHFD-fed $Gsk3\beta^{\Delta Hep}$ mice and $Gsk3\beta^{fl/fl}$ mice (*left panel*) and quantification of GPX4 protein normalized to vinculin (*right panel*). Bar graphs represent the mean ± SD; **** $P < .0001$, ns, nonsignificant (1-way ANOVA with Bonferroni's multiple comparison).

exhibit normal metabolic characteristics and insulin signaling without evidence of liver necrosis.[59] Knockdown efficacy was assessed by Western blotting for GSK3β. $Gsk3\beta^{fl/fl}$ mice were used as the controls. FFC-fed mice were injected with vehicle or the GSK3 inhibitor LY intraperitoneally at 10 mg/kg body weight/dose 3 times a week at the age of 20 weeks of diet for 4 weeks. CDHFD-fed mice were administered Elraglusib (9-ING-41) via intraperitoneal injection at 30 mg/kg/day during the final 2 weeks of the diet. All the mice used had a C57Bl/6J background. $Gsk3\beta^{fl/fl}$ and $Gsk3\beta^{\Delta Hep}$ mice were cohoused at the Mayo Clinic Rochester animal facility with a 12-hour light-dark cycle. All experimental interventions were performed during the light cycle. The use of anesthetics in the experimental mice was conducted according to the IACUC guidelines.

Diet-induced Murine MASH Models

Male $Gsk3\beta^{fl/fl}$ and $Gsk3\beta^{\Delta Hep}$ mice were subjected to experimental feeding studies at 8 weeks of age. The chow diet was standard rodent diet (5053 PicoLab Rodent Diet 20; LabDiet) using tap water. We employed 2 mouse models of MASH: the FFC diet and the CDHFD. The male mice were fed an FFC diet for 24 weeks to induce MASH. The FFC diet consisted of 40% energy as fat (12% saturated fatty acid, 0.2% cholesterol) (AIN-76A Western Diet, Test-Diet), fructose (23.1 g/L), and glucose (18.9 g/L) in drinking water. MASH induced by an FFC diet closely mimics the human disease phenotype and associated metabolic syndrome and has been extensively validated.[60,61] We also employed the CDHFD diet (A06071302, Research Diet), which consists of 60% fat, 0.1% methionine, and no added choline, and fed 8-week-old mice for 6

Figure 12. (***See previous page***). **Pharmacological inhibition of GSK3 reduces liver ferroptosis in murine MASH.** (*A*) mRNA expression of acyl-CoA synthetase long-chain family member 4 (*Acsl4*) and prostaglandin-endoperoxide synthase 2 (*Ptgs2*) (n = 4–5 per group). (*B*) Immunohistochemical staining of oxPAPC, 4-HNE, and TFRC in liver sections from chow- and FFC-fed wild type mice treated with vehicle and LY (*left panels*). oxPAPC and 4-HNE-positive cells were quantified in 5 random 20× microscopic fields and averaged for each animal (*right panels*). TFRC-positive area was quantified in 5 random 20× microscopic fields and averaged for each animal (*right panel*) (n = 4–5 per group). (*C*) Representative staining for 4-HNE (normal, n = 4; simple steatosis, n = 5; MASH, n = 5) and hyperoxidized PRDX3 (normal, n = 4; simple steatosis, n = 4; MASH, n = 6) and quantification of the positively stained area in patients with MASH vs simple steatosis and healthy controls. Bar graphs represent the mean ± SD; * $P < .05$, ** $P < .01$, *** $P < .001$, **** $P < .0001$, ns, nonsignificant (2-way ANOVA with Bonferroni's multiple comparison). Scale bar: 20 μm (*B, C*).

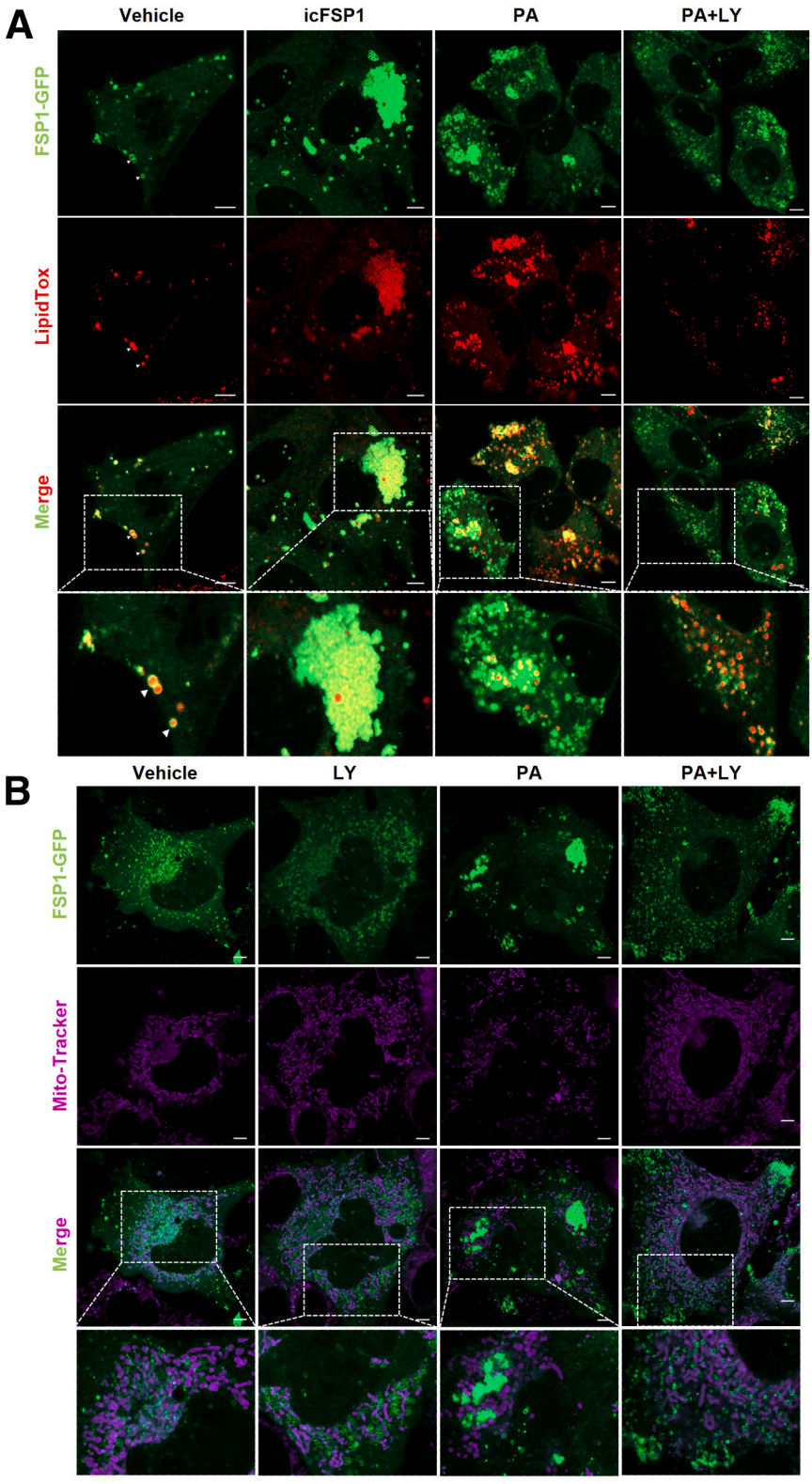

Figure 14. GSK3β inhibition in hepatocytes under lipotoxic stress reduces FSP1 condensation. (*A*) Representative fluorescence images of hFSP1–EGFP–Strep-transfected Huh7 cells treated with 2.5 μM icFSP1 and 500 μM PA ± 100 nM LY. Cells were stained with LipidTox (*red*) to label LDs. (*B*) Representative fluorescence images of hFSP1–EGFP–Strep-transfected Huh7 cells treated with 100 nM LY or 500 μM PA ± 100 nM LY. The cells were stained with MitoTracker (DsRed) to label mitochondria. Scale bar: 5 μm (*A*, *B*).

weeks. CDHFD-fed male mice experienced minimal body weight loss compared with those fed a traditional methionine and choline-deficient (MCD) diet. CDHFD effectively recapitulates the histopathological features of human MASH in terms of hepatic steatosis, elevated ALT levels, hepatic inflammation, and fibrosis, as demonstrated in previous studies.[60,61] Because sex is a biological variable, we justify the use of male mice as follows: male mice are more prone to

high-fat diet-induced obesity[62,63] and MASH.[24] In contrast, female mice do not develop a comparable body weight gain and histological features of MASH with fibrosis when fed a diet rich in FFC or other high-fat diets.[64,65]

Cells

AML12 cells were purchased from ATCC and cultured in Dulbecco's modified Eagle's medium (DMEM/F12) supplemented with 10% fetal bovine serum (FBS), ITS

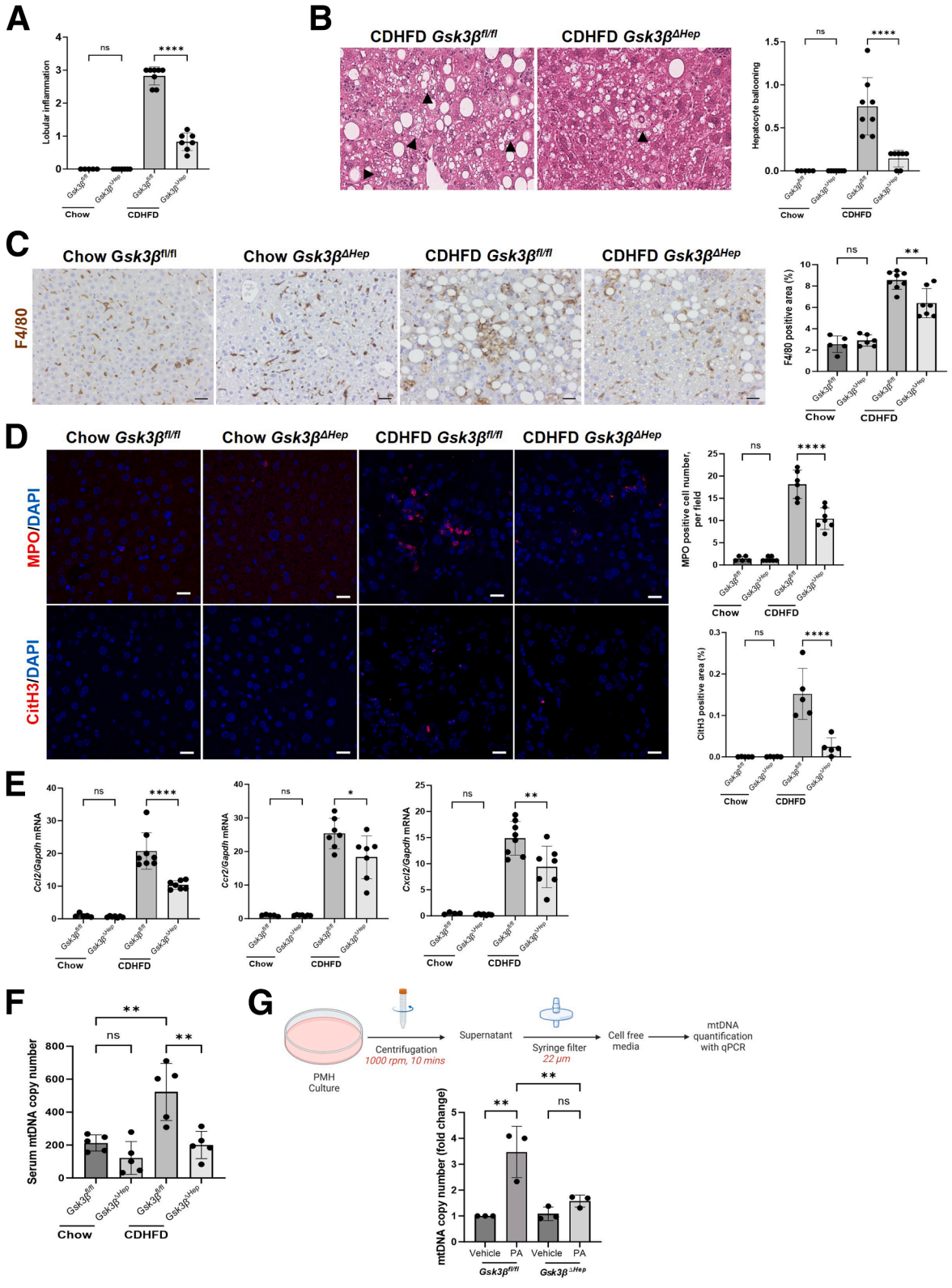

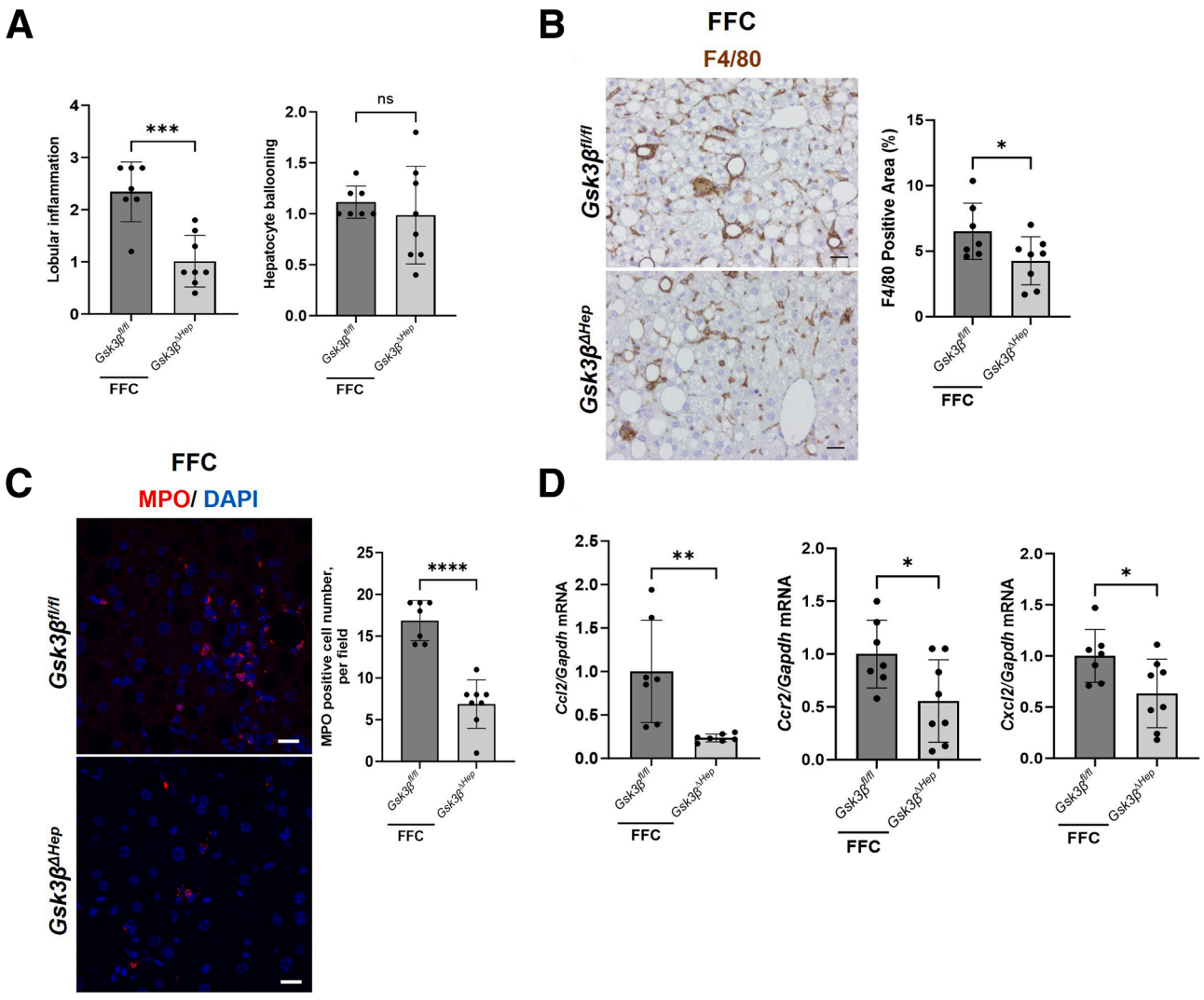

Figure 16. Hepatocyte-specific *Gsk3β* deletion reduces liver inflammation in FFC-induced murine MASH. (*A*) Lobular inflammation and hepatocyte ballooning components of NAS in FFC-fed mice were quantified in 5 random 20× microscopic fields and averaged for each animal (n = 5–8 per group). (*B*) Immunohistochemistry staining for F4/80 on liver sections from *Gsk3β*$^{\Delta Hep}$ mice and *Gsk3β*$^{fl/fl}$ mice (*left*). The F4/80-positive area was quantified in 5 random 10× microscopic fields and averaged for each animal (*right*) (n = 7–8 per group). (*C*) MPO immunofluorescent staining (*red*) in liver sections from *Gsk3β*$^{\Delta Hep}$ mice and *Gsk3β*$^{fl/fl}$ mice, with nuclei stained using DAPI (*blue*) (*left*). MPO-positive area was quantified in 5 random 10× microscopic fields and averaged for each animal (*right*) (n = 7–8 per group). (*D*) mRNA expression of C-C motif ligand 2 (*Ccl2*), C-C chemokine receptor type 2 (*Ccr2*), and C-X-C motif chemokine ligand 2 (*Cxcl2*) (n = 7–8 per group). Bar graphs represent the mean ± SD; * $P < .05$, ** $P < .01$, *** $P < .001$, **** $P < .0001$, ns, nonsignificant (1-way ANOVA with Bonferroni's multiple comparison and unpaired *t*-test). Scale bar: 20 μm (*B, C*).

Figure 15. (*See previous page*). Hepatocyte-specific *Gsk3β* deletion reduces liver inflammation in CDHFD-induced murine MASH. (*A*) Lobular inflammation component of NAS in CDHFD-fed mice was quantified in 5 random 20× microscopic fields and averaged for each animal (n = 5–8 per group). (*B*) Representative images and averaged quantification of hepatocyte ballooning component of NAS in CDHFD-fed mice in 5 random 20× microscopic fields per animal (n = 5–8 per group). (*C*) Immunohistochemical staining for F4/80 in liver sections from *Gsk3β*$^{\Delta Hep}$ and *Gsk3β* $^{fl/fl}$ mice (*left panel*). F4/80-positive area was quantified in 5 random 10× microscopic fields and averaged for each animal (*right*) (n = 5–8 per group). (*D*) Immunofluorescence staining for MPO and CitH3 (*red*) in liver sections from *Gsk3β*$^{\Delta Hep}$ and *Gsk3β* $^{fl/fl}$ mice, with nuclei stained using DAPI (*blue*) (*left panel*). MPO and CitH3-positive areas were quantified in 5 random 10× microscopic fields and averaged for each animal (*right*) (n = 5–8 per group). (*E*) mRNA expression of C-C motif chemokine ligand 2 (*Ccl2*), C-C chemokine receptor type 2 (*Ccr2*), and C-X-C motif chemokine ligand 2 (*Cxcl2*) (n = 5–8 per group). (*F*) Quantification of relative mtDNA copy numbers per 100 μL of serum sample (n = 5 per group). (*G*) Quantification of mtDNA release in the cell culture medium of *Gsk3β*$^{\Delta Hep}$ and *Gsk3β* $^{fl/fl}$ PMHs. mtDNA levels are expressed as fold changes (n = 3). Bar graphs represent the mean ± SD; * $P < .05$, ** $P < .01$, **** $P < .0001$, ns, nonsignificant (1-way ANOVA with Bonferroni's multiple comparison). Scale bar: 20 μm (*C, D*).

supplement (insulin, 10 μg/mL; transferrin: 5.5 μg/mL, selenium, 5 ng/mL), dexamethasone (40 ng/mL), and 1% primocin (InvivoGen). The human hepatocellular carcinoma Huh7 cells were cultured in DMEM supplemented with 10% FBS and 1% primocin. Primary mouse hepatocytes were isolated using collagenase perfusion and Percoll density gradient centrifugation as previously described.[27,66] Briefly, the liver was digested with

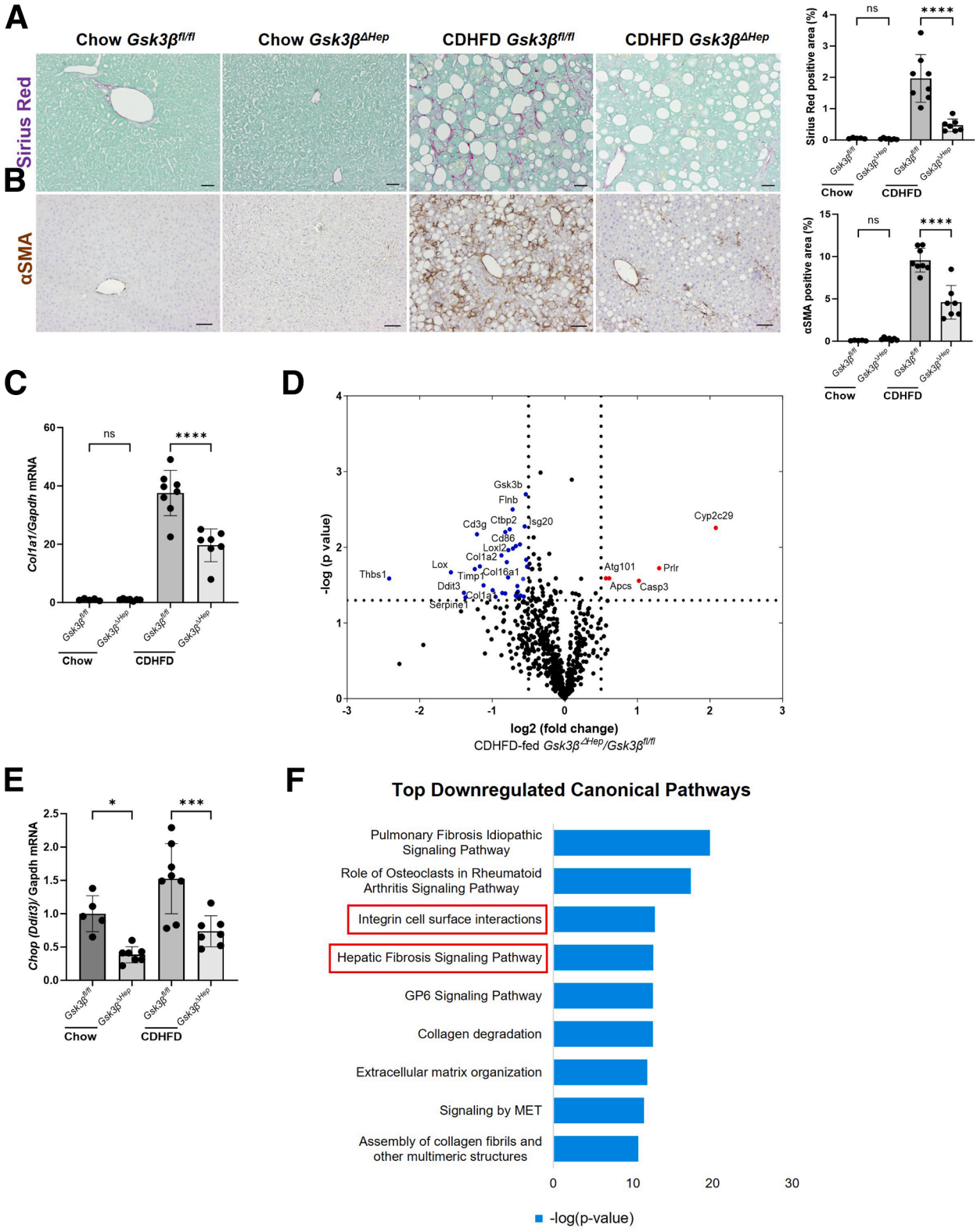

collagenase infused via the portal vein, and the obtained cell suspension was filtered through a 70-μm cell strainer to remove debris. The filtered suspension was centrifuged at 50 g for 2 minutes at 4°C. The pellet containing hepatocytes was resuspended in DMEM, layered with 90% Percoll solution, and centrifuged at 100× g for 10 minutes to separate hepatocytes from NPCs. The PMH were cultured in DMEM supplemented with 10% FBS, 100 ng/mL insulin, and 1% primocin (InvivoGen). AML12 cells were seeded at a density of 2.5×10^5 cells/well in 6-well plates. Upon reaching 70% to 80% confluence, cells were treated with either 500 μM PA to induce lipotoxicity ± 100 nM of the GSK3 inhibitor LY, or vehicle (isopropanol or dimethyl sulfoxide [DMSO]).

Assessment of Metabolic Profiles in Mice

A CLAMS (Columbus Instruments) was used to measure the metabolic parameters, including oxygen consumption, carbon dioxide production, and respiratory exchange ratio. Physical activity was measured using sensors in the calorimetry chambers. The lean vs fat body composition was assessed using echo-magnetic resonance imaging (MRI). Blood glucose and plasma insulin levels were measured using Assure 4 (Arkray) and Ultra-Sensitive Mouse Insulin enzyme-linked immunosorbent assay (ELISA) kits (Crystal Chem Inc), respectively. HOMA-IR was calculated using the following formula: HOMA-IR = 26 × fasting insulin level (ng/mL) × fasting glucose level (mg/dL)/405.[27]

Measurement of Liver TG and ALT Levels

Liver TG levels were measured in the liver specimens. Fifty milligrams of liver tissue were homogenized in a 5% NP-40 solution. Tissue homogenates were boiled twice and centrifuged at 20,000g for 2 minutes. The extracted triglycerides were diluted and quantified using an EnzyChrom Triglyceride Kit (BioAssay System) according to the manufacturer's instructions. Photometric absorbance was measured at 570 nm using a Synergy H1 microplate reader (BioTek). The VetScan2 system (Abaxis Veterinary Diagnostics) was used to measure serum ALT levels.

Fluorometric Measurement of Liver MDA Levels

Liver MDA levels were measured using the Lipid Peroxidation (MDA) Assay Kit (Sigma-Aldrich, MAK085). Tissue samples (10 mg) were homogenized in 2N perchloric acid (Sigma-Aldrich, #244252) on ice, and the homogenate was processed following the manufacturer's protocol. MDA levels were quantified by measuring the absorbance of the MDA-TBA adduct fluorescence at λEx/λEm = 530/560 nm using a Synergy H1 microplate reader (BioTek). Concentrations were determined using a standard curve and normalized to the tissue weight.

Colorimetric Measurement of Liver NAD^+ Levels

Liver NAD^+ levels were measured using NAD/NADH Assay Kit (Colorimetric) (ab65348). Briefly, 20 mg of frozen liver tissue was homogenized in 400 μL of NAD/NADH Extraction Buffer on ice and centrifuged at top speed for 5 minutes at 4°C to remove insoluble material. Samples were filtered through a 10-kDa Spin Column (ab93349) before performing the assay. All subsequent procedures were carried out according to the manufacturer's instructions. After incubation at room temperature for 2 hours, absorbance was measured at 450 nm using a Synergy H1 microplate reader (BioTek). Concentrations were determined using a standard curve and normalized to the tissue weight.

Histological, Immunohistochemical, and Digital Imaging Analyses

Deidentified human liver tissues were obtained through liver biopsy or surgical hepatic resection from patients with normal liver, isolated steatosis, or MASH (Institutional Review Board #22-000320). H&E staining was performed on the murine liver samples to visualize and assess histopathological changes. The NAS, a semi-quantitative score used to evaluate the severity of liver pathology in murine models that accounts for steatosis, ballooned hepatocytes, and lobular inflammation, was used to assess the liver samples.[67] Sirius red staining was performed as previously described.[68] Sirius red-stained tissue was imaged using a light microscope, and the tissue area was determined using the ImageJ software. Formalin-fixed paraffin-embedded mouse or human liver tissue sections were deparaffinized, hydrated, and stained with antibodies against F4/80 (1:500), α-SMA (1:1,000), oxPAPC (1:1,000), 4HNE (1:1,000), GS (1:2,000), CYP2F2 (1:100), TFRC (1:500), NAMPT (1:200 IHC, 1:50 IF), $SO_{2/3}$- PRDX3 (1:100), Cit-H3 (1:100). The bound antibody was detected using a Vectastain ABC kit for goat (PK-6105 or PK-6101, Vector Laboratories) and diaminobenzidine (DAB) substrate (Vector Laboratories) according to the manufacturer's instructions.

Figure 17. (*See previous page*). Hepatocyte-specific *Gsk3β* deletion attenuates liver fibrosis in CDHFD-induced murine MASH. (*A*) Representative images of Sirius Red staining (*right panel*). Sirius Red-positive areas were quantified in 5 random 10× microscopic fields and averaged for each animal (*left panel*) (n = 5–8 per group). (*B*) Immunohistochemical staining for αSMA in *Gsk3β*$^{\Delta Hep}$ and *Gsk3β*$^{fl/fl}$ mice (*right panel*). αSMA-positive areas were quantified in 5 random 10× microscopic fields and averaged for each animal (*left panel*) (n = 5–8 per group). (*C*) mRNA expression of collagen 1a1 (*Col1a1*) (n = 5–8 per group). (*D*) Volcano plot showing differentially expressed genes ($P < .05$) in CDHFD-fed *Gsk3β*$^{\Delta Hep}$ mice vs *Gsk3β*$^{fl/fl}$ mice using the NanoString nCounter Fibrosis Panel on liver tissue RNA (n = 3 per group). The X- and Y-axes represent the log 2-fold change (log_2FC) and -log (*P* value) of the genes, respectively. *Red and blue circles* indicate the upregulated and downregulated genes, respectively. (*E*) mRNA expression of C/EBP homologous protein (*Chop*) (n = 5–8 per group). (*F*) IPA analysis of NanoString Fibrosis Panel data showing the top downregulated canonical pathways in CDHFD-fed *Gsk3β*$^{\Delta Hep}$ mice compared with *Gsk3β*$^{fl/fl}$ mice. Bar graphs represent the mean ± SD; * $P < .05$, *** $P < .001$, **** $P < .0001$, ns, nonsignificant (1-way ANOVA with Bonferroni's multiple comparison). Scale bars: 20 μm (*A*) and 50 μm (*B*).

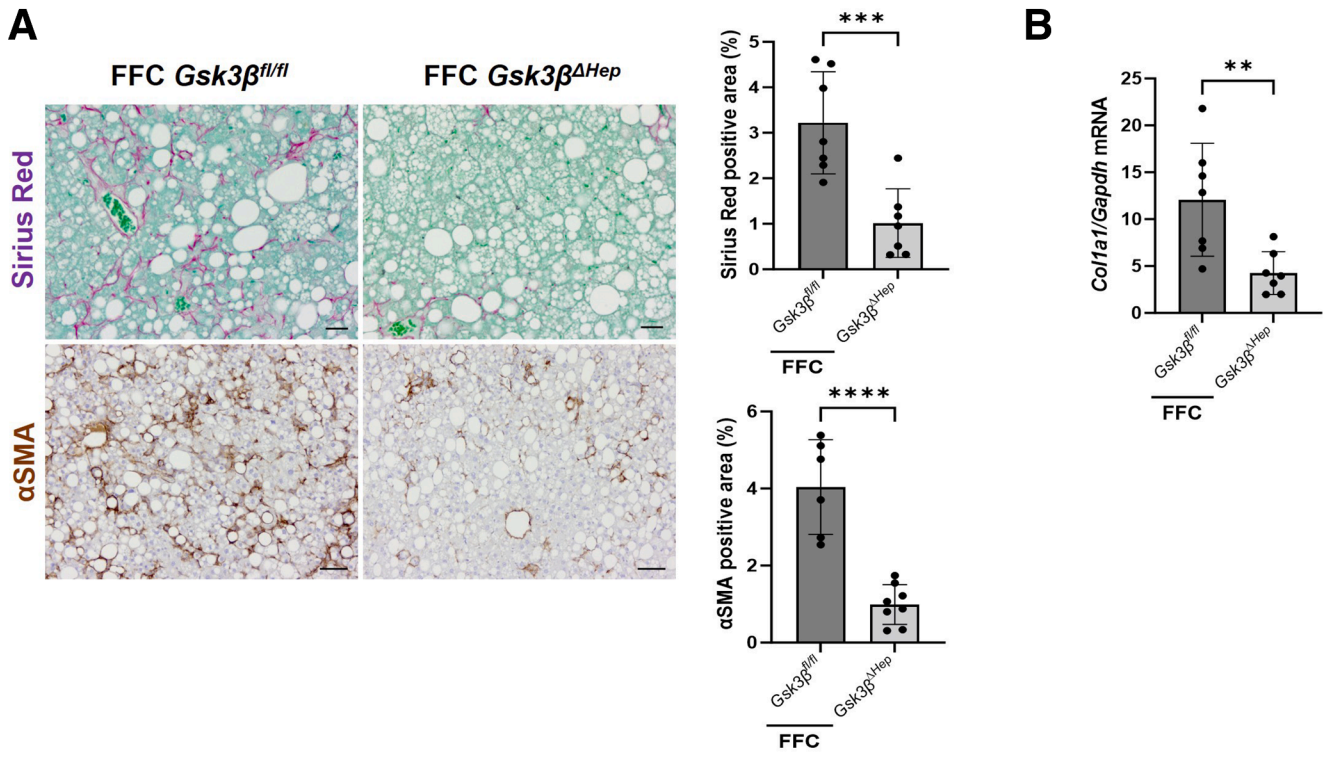

Figure 18. Hepatocyte-specific *Gsk3β* deletion attenuates liver fibrosis in FFC-induced murine MASH. (*A*) Representative images of Sirius Red staining (*top*) and immunohistochemical staining for αSMA from FFC-fed *Gsk3β*$^{\Delta Hep}$ and *Gsk3β*$^{fl/fl}$ mice (*bottom*). Sirius Red-positive areas were quantified in 5 random 10× microscopic fields and averaged for each animal (*right*) (n = 7–8 per group). αSMA-positive areas were quantified in 5 random 10× microscopic fields and averaged for each animal (right) (n = 7–8 per group). (*B*) mRNA expression of collagen 1a1 *(Col1a1*) (n = 7 per group). Bar graphs represent mean ± SD, ** $P < .01$, *** $P < .001$, **** $P < .0001$, ns, nonsignificant (unpaired *t*-test). Scale bars: 20 μm (*top*) and 50 μm (*bottom*).

The tissue sections were counterstained with hematoxylin. MPO staining was evaluated by immunofluorescence using an anti-goat alexa-568 secondary antibody (#A-11057, Thermo Fisher Scientific). Cit-H3, NAMPT, and $SO_{2/3}$-PRDX3 staining were evaluated by immunofluorescence with an anti-rabbit alexa-568 secondary antibody (A10042, Thermo Fisher Scientific). Cell death in murine liver tissues was assessed using the ApopTag Peroxidase In Situ Cell Death Detection Kit (Millipore Sigma) according to the manufacturer's instructions.

Zonal Quantification of Steatosis

H&E-stained slides were scanned using an Aperio AT2 scanner (Leica Biosystems) at 40× magnification at the Pathology Research Core, Mayo Clinic. Central vein (CV) and portal vessels (PVs) were annotated using Qupath 0.4.[69] A nonlinear boundary between different zones was acquired using nonlinear regression, showing the anatomical distance to the boundary annotations of both CV and PV. A Gaussian process (GP) regression was used to predict the target value of −1 on the CV boundary contours and +1 on the PV boundary. A topographic map was constructed with 3 boundaries between zones determined by the level curve with a GP output of −0.5 and +0.5, which partitions the tissue between CV and PV into 3 zones. Whole slide image analysis included detailed quantification of LD size within each of the defined zones, performed using a machine learning algorithm trained on human liver biopsies,[70] providing a quantitative assessment of lipid distribution across the different zones of the liver lobule.

NanoString-based Gene Expression Profiling

Gene expression profiles of murine bulk liver tissues were assessed using the NanoString nCounter system (NanoString Technologies). We employed a Metabolic Profiling Panel of liver tissues from FFC-fed mice and a fibrosis panel of liver tissues from CDHFD-fed mice. The Metabolic Profiling Panel consisted of 768 genes across 34 annotated pathways, whereas the fibrosis panel included 770 genes across 51 annotated pathways. Total RNA was isolated from murine liver tissues using the Zymo Research Direct-zol RNA MiniPrep Kit (Zymo Research) according to the manufacturer's instructions. The quantity and quality of extracted RNA were assessed using a NanoDrop spectrophotometer (Thermo Fisher Scientific). For the NanoString nCounter assay, 100 ng of total RNA was hybridized at 65°C for 18 hours in a thermal cycler with a custom-designed code set specific for the target genes of interest, including housekeeping genes for normalization, according to the manufacturer's instructions. Raw data were normalized to internal positive controls and housekeeping genes to account for the variability in RNA input and hybridization

efficiency. Data analysis was performed using nSolver Analysis Software (NanoString Technologies). Differential gene expression analysis was performed to identify significant differences between the experimental groups.

NEFA and Total FA Composition

Liver tissue was homogenized in 1 × phosphate buffered saline (PBS) after adding 10 μL of PBS to 1 mg of tissue prior to extraction. FAs and total FA composition were measured against a standard curve on a triple quadrupole mass spectrometer coupled with an Ultra Pressure Liquid Chromatography system (LC/MS), as previously described.[71] Briefly, 50 μL of homogenate was spiked with an internal standard before extraction with methyl tertiary-butyl ether (MTBE). Approximately 25% of the sample was dried, hydrolyzed, re-extracted, and brought up in running buffer for the analysis of the total FA composition. The remaining portion of the extract was dried and brought up in running buffer prior to injection into the LC/MS for NEFA measurement. Data acquisition was performed under negative electrospray ionization conditions.

Transmission Electron Microscopy

Liver tissues were fixed with Trump's EM Fixative (4% paraformaldehyde + 1% glutaraldehyde in 0.1 mol/L PBS, pH 7.2). After fixation, the tissues were stained with 1% osmium tetroxide, washed with distilled water, stained with 2% uranyl acetate, dehydrated through a graded series of ethanol and acetone, and embedded in Embed 812 resin (EMS). Following a 24-hour polymerization at 60°C, 0.1-μm ultrathin sections were prepared and poststained with lead citrate. Micrographs were acquired using a JEOL 1400 Plus transmission electron microscope (JEOL, Inc) at 80 kV, equipped with a Gatan Orius camera (Gatan, Inc). ImageJ software was used to measure mitochondrial morphology. Mitochondria-LD contacts were defined as mitochondria juxtaposed to LDs at <100 nm.

Seahorse Assay

A Seahorse XF Analyzer (Agilent Technologies) was used to assess mitochondrial bioenergetics in primary mouse hepatocytes and AML12 cells. Prior to the assay, assay cartridges were hydrated in a Seahorse XF Calibrant at 37°C in a non-CO_2 incubator overnight. Primary mouse hepatocytes were seeded at a density of 15,000 cells/well in Seahorse XF96 cell culture microplates coated with collagen I. AML12 cells were cultured at a density of 20,000 cells/well. The cells were allowed to adhere overnight at 37°C in a 5% CO_2 incubator. The cells were washed and incubated in Seahorse XF Assay Medium (Agilent Technologies) supplemented with 25 mM glucose, 1 mM pyruvate, and 2 mM glutamine at 37°C in a non-CO_2 incubator for 1 hour prior to the start of the assay. 1 μM oligomycin, 0.25 μM FCCP, and 1 μM rotenone-antimycin-A were loaded into the assay wells. The OCR and extracellular acidification rate (ECAR) for each well were recorded and reported as pmol/min and mpH/min, respectively. Results are displayed as a percentage of maximal OCR and ECAR or as relative fold change of each parameter between time points.

qRT-PCR

Total RNA was isolated using the Zymo Research Direct-zol RNA MiniPrep Kit (Zymo Research) following the manufacturer's protocol. For cDNA synthesis, 1 μg of total RNA was reverse transcribed using the LightCycler 480 SYBR Green I Master (Roche Diagnostics) according to the manufacturer's instructions. The resulting cDNA was diluted 1:5 with nuclease-free water and was used as a template for qRT-PCR. Gene expression was quantified by real-time PCR using SYBR green fluorescence on a LightCycler 480 instrument (Roche Applied) (Primers are listed in Table 1). Target gene expression was calculated and normalized using the $^{\Delta\Delta}$Ct method.

Immunoblot Analysis

Mouse liver tissues were homogenized in T-PER lysis buffer (#78510; Roche) containing protease and phosphatase inhibitors (#78442; Thermo Scientific). Cells were lysed using radioimmunoprecipitation assay (RIPA) buffer (50 mM Tris-HCl, pH 7.4; 1% Nonidet P-40; 0.25% sodium deoxycholate; 150 mM NaCl; 1 mM EDTA with protease inhibitors). The homogenates were centrifuged at 15,000× g for 15 minutes at 4°C to remove debris, and the supernatants were collected. Protein concentration was quantified using the Bradford assay (Sigma-Aldrich). Equal amounts of protein were loaded onto sodium dodecyl sulfate (SDS)-sulfate-polyacrylamide gel electrophoresis (PAGE) gels and then transferred to nitrocellulose membranes (Bio-Rad). Following transfer, the membranes were blocked in 5% nonfat dry milk in Tris-buffered saline with 0.1% Tween-20 (TBST) for 1 hour at room temperature. Membranes were then incubated overnight at 4°C with primary antibody of interest diluted in 5% bovine serum albumin (BSA) or 5% non-fat dry milk in TBST. The 4-HNE primary antibody was used at a 1:4,000 dilution, while the GPX4 antibody was applied at a 1:1,500 dilution. All other primary antibodies were used at a dilution of 1:1,000 unless otherwise recommended by the manufacturer. After primary antibody incubation, membranes were washed 3 times with TBST and incubated with horseradish peroxidase (HRP)-conjugated secondary antibodies against rabbit (Alpha Diagnostic International) or mouse (Southern Biotech) (1:5000 dilution) in 5% nonfat dry milk in TBST for 1 hour at room temperature. Following incubation with the secondary antibody, the membranes were washed 3 times with TBST. Protein bands were visualized using enhanced chemiluminescence (ECL) detection reagents (GE Healthcare). GAPDH and Vinculin were used as loading controls. Band intensities were quantified using ImageJ software and normalized to GAPDH and Vinculin levels.

Viability Assay Using Celigo Imaging Cytometer

AML12 cells were seeded in Corning 3603 96-well plates at a density of 10,000 cells/well and allowed to adhere overnight. The cells were then treated with PA, Fer-

Table 1. PCR Primers

Primer	Sequence
Mouse *Ccr2* forward primer	ATCCACGGCATACTATCAACATC
Mouse *Ccr2* reverse primer	CAAGGCTCACCATCATCGTAG
18S forward primer	CGCTTCCTTACCTGGTTGAT
18S reverse primer	GAGCGACCAAAGGAACCATA
Mouse *Col1a1* forward primer	GCTCCTCTTAGGGGCCACT
Mouse *Col1a1* reverse primer	CCACGTCTCACCATTGGGG
Mouse *Cxcl2* forward primer	CCAACCACCAGGCTACAGG
Mouse *Cxcl2* reverse primer	GCGTCACACTCAAGCTCTG
Mouse *Plin5* forward primer	TGTCCAGTGCTTACAACTCGG
Mouse *Plin5* reverse primer	CAGGGCACAGGTAGTCACAC
Mouse *Fsp1* forward primer	CTGCCTACCGCAGTGCATT
Mouse *Fsp1* reverse primer	ACGCCATCATTTCTGCCCA
Mouse *Tfam* forward primer	ATTCCGAAGTGTTTTTCCAGCA
Mouse *Tfam* reverse primer	TCTGAAAGTTTTGCATCTGGGT
Mouse *Gapdh* forward primer	CCA CCC CAG CAA GGA GAC T
Mouse *Gapdh* reverse primer	GAA ATT GTG AGG GAG ATG CT
Mouse *Ppargc1a* forward primer	TGAGGACCGCTAGCAAGTTT
Mouse *Ppargc1a* reverse primer	TGAAGTGGTGTAGCGACCAA
Mouse *Acsl4* forward primer	CTC ACC ATT ATA TTG CTG CCT GT
Mouse *Acsl4* reverse primer	TCT CTT TGC CAT AGC GTT TTT CT
Mouse *Srebf1* forward primer	GGAGCCATGGATTGCACATT
Mouse *Srebf1* reverse primer	GGCCCGGGAAGTCACTGT
Mouse *Fth1* forward primer	CAA GTG CGC CAG AAC TAC CA
Mouse *Fth1* reverse primer	GCC ACA TCA TCT CGG TCA AAA
Mouse *Ptgs2* forward primer	TGA GCA ACT ATT CCA AAC CAG C
Mouse *Ptgs2* reverse primer	GCA CGT AGT CTT CGA TCA CTA TC
Mouse *Gpx4* forward primer	GAT GGA GCC CAT TCC TGA ACC
Mouse *Gpx4* reverse primer	CCC TGT ACT TAT CCA GGC AGA
Mouse *Ccl2* forward primer	TTAAAAACCTGGATCGGAACCA
Mouse *Ccl2* reverse primer	GCATTAGCTTCAGATTTACGGG
Mouse *Chop* forward primer	CTGCCTTTCACCTTGGAGAC
Mouse *Chop* reverse primer	CGTTTCCTGGGGATGAGATA

PCR, polymerase chain reaction.

1, or LY. Following the treatment period, cell viability was assessed using a Celigo Imaging Cytometer (Nexcelom Bioscience) by staining the cells with a combination of propidium iodide (PI) and Hoechst 33342 dye (ViaStain Hoechst/PI, Cat. # CSK-V0005-1). Hoechst 33342 was used to stain all nuclei (total cell count), whereas PI selectively stained dead cells. The viability was calculated as the percentage of viable cells.

Live Cell Imaging

Mitochondrial staining was performed using Mito-Tracker Green (Thermo Fisher Scientific, #CST9074, 1:3000) to label active mitochondria. AML12 cells were washed with PBS and incubated with 100 nM MitoTracker and Hochest (33342 (1:1000) in PBS for 30 minutes at 37°C. After incubation, the cells were washed 3 times with PBS to remove excess dye. LDs were stained using LipidTox Neutral Lipid Stain (Thermo Fisher Scientific, #34477, 1:3000). Images were captured using a C-Apochromat 63_ objective/1.20 W korrM27 of a fluorescence confocal microscope (LSM980 AxioObserver, Carl Zeiss) and processed using the Zen Lite software (Carl Zeiss).

Plasmid Transfection

hFSP1-GFP-Strep plasmid was a gift from Dr Marcus Conrad. Huh7 cells were transfected with 2.5 μg of hFSP1-GFP-Strep plasmid DNA using Lipofectamine 3000 reagent (Thermo Fisher Scientific) according to the manufacturer's protocol. After transfection, the medium was replaced after 24 hours, and the cells were further incubated for 24 hours before selection. To obtain stable cells, the cells were selected using blasticidin (15 ug/mL). SPLICSFAST-LDh-MT-P2A (Addgene plasmid #214896; http://n2t.net/addgene:214896; RRID: Addgene_214896) was a gift from Dr Tito Calì. For experiments with the LD-mitochondria sensor SPLICSs (short-range LD-mitochondria interactions), AML12 cells were transfected with FuGENE HD reagent (Promega), according to the manufacturer's protocol. After 72 hours, cells were seeded in chamber slide and treated with PA ± LY overnight. Cells were stained with MitoTracker Deep Red (Invitrogen, #M22426, 1:3000) and examined by confocal microscope (LSM980 AxioObserver, Carl Zeiss) and processed using the Zen Lite software (Carl Zeiss). Quantification was performed with ImageJ software.

mtDNA Quantification

Total DNA was extracted from serum samples or hepatocyte-conditioned medium using the QIAamp DNA Blood Mini Kit (QIAGEN) according to the manufacturer's protocol with minor modifications. To optimize the DNA yield, the elution step was performed using 30 μL elution buffer. Extracted DNA was quantified using a NanoDrop Spectrophotometer. mtDNA was quantified using ScienCell's Absolute Mouse Mitochondrial DNA Copy Number Quantification qPCR Assay Kit (#M8948). mtDNA copy number was calculated using the $^{\Delta\Delta}$Ct method and normalized to the sample volume (copy number/μL).

Bioinformatics Analysis

Genes with a threshold of $P < .05$ were subjected to upstream regulator and pathway analysis using the IPA platform (Qiagen). IPA was performed on NanoString Metabolic and Fibrosis Panels. The significance of the association between the genes from the dataset and the canonical pathways was determined based on the enrichment ratio (number of genes mapped to a given pathway divided by the total number of molecules in the canonical pathway) and Fisher's exact test P value. Predictable activation or inhibition states of the identified canonical pathways were identified using activation z-scores, based on accessible datasets in the ingenuity knowledge base.

Statistical Analysis

Statistical analyses were performed using GraphPad Prism software (version 9.2.0; GraphPad Software). Data are presented as mean ± standard deviation (SD). For comparisons among multiple groups, a 1-way analysis of variance (ANOVA) followed by Bonferroni's multiple comparison test was performed. Unpaired 2-tailed Student's *t*-test was used for comparisons between the two groups. *, **, ***, and **** indicate statistical significance with $P < .05$, $P < .01$, $P < .001$, and $P < .0001$, respectively. Statistically nonsignificant results were labeled as ns, where appropriate.

Supplementary Material

Note: To access the supplementary material accompanying this article, visit the full text version at https://doi.org/10.1016/j.jcmgh.2025.101633.

References

1. Younossi ZM, Golabi P, Paik JM, et al. The global epidemiology of nonalcoholic fatty liver disease (NAFLD) and nonalcoholic steatohepatitis (NASH): a systematic review. Hepatology 2023;77:1335–1347.
2. Neuschwander-Tetri BA. Hepatic lipotoxicity and the pathogenesis of nonalcoholic steatohepatitis: the central role of nontriglyceride fatty acid metabolites. Hepatology 2010;52:774–788.
3. Friedman SL, Neuschwander-Tetri BA, Rinella M, Sanyal AJ. Mechanisms of NAFLD development and therapeutic strategies. Nat Med 2018;24:908–922.
4. Hirsova P, Gores GJ. Death receptor-mediated cell death and proinflammatory signaling in nonalcoholic steatohepatitis. Cell Mol Gastroenterol Hepatol 2015;1:17–27.
5. Inaba Y, Hashiuchi E, Watanabe H, et al. The transcription factor ATF3 switches cell death from apoptosis to necroptosis in hepatic steatosis in male mice. Nat Commun 2023;14:167.
6. Koh EH, Yoon JE, Ko MS, et al. Sphingomyelin synthase 1 mediates hepatocyte pyroptosis to trigger nonalcoholic steatohepatitis. Gut 2021;70:1954–1964.
7. Tsurusaki S, Tsuchiya Y, Koumura T, et al. Hepatic ferroptosis plays an important role as the trigger for initiating inflammation in nonalcoholic steatohepatitis. Cell Death Dis 2019;10:449.
8. Jiang X, Stockwell BR, Conrad M. Ferroptosis: mechanisms, biology and role in disease. Nat Rev Mol Cell Biol 2021;22:266–282.
9. Xie Y, Hou W, Song X, et al. Ferroptosis: process and function. Cell Death Differ 2016;23:369–379.
10. Feng F, He S, Li X, et al. Mitochondria-mediated ferroptosis in diseases therapy: from molecular mechanisms to implications. Aging Dis 2024;15:714–738.
11. Zadoorian A, Du X, Yang H. Lipid droplet biogenesis and functions in health and disease. Nat Rev Endocrinol 2023;19:443–459.
12. Talari NK, Mattam U, Meher NK, et al. Lipid-droplet associated mitochondria promote fatty-acid oxidation through a distinct bioenergetic pattern in male Wistar rats. Nat Commun 2023;14:766.
13. Nguyen TB, Louie SM, Daniele JR, et al. DGAT1-dependent lipid droplet biogenesis protects mitochondrial function during starvation-induced autophagy. Dev Cell 2017;42:9–21.e5.
14. Benador IY, Veliova M, Mahdaviani K, et al. Mitochondria bound to lipid droplets have unique bioenergetics, composition, and dynamics that support lipid droplet expansion. Cell Metab 2018;27:869–885.e6.
15. Vonderlin J, Chavakis T, Sieweke M, Tacke F. The multifaceted roles of macrophages in NAFLD pathogenesis. Cell Mol Gastroenterol Hepatol 2023;15:1311–1324.
16. Yang Y, Wang Y, Guo L, et al. Interaction between macrophages and ferroptosis. Cell Death Dis 2022;13:355.
17. Beurel E, Grieco SF, Jope RS. Glycogen synthase kinase-3 (GSK3): regulation, actions, and diseases. Pharmacol Ther 2015;148:114–131.
18. Jeffers A, Qin W, Owens S, et al. Glycogen synthase kinase-3β inhibition with 9-ING-41 attenuates the progression of pulmonary fibrosis. Sci Rep 2019;9:18925.
19. Ramirez SH, Fan S, Zhang M, et al. Inhibition of glycogen synthase kinase 3beta (GSK3beta) decreases inflammatory responses in brain endothelial cells. Am J Pathol 2010;176:881–892.
20. Wang L, Ouyang S, Li B, et al. GSK-3β manipulates ferroptosis sensitivity by dominating iron homeostasis. Cell Death Discov 2021;7:334.
21. Wu X, Liu C, Li Z, et al. Regulation of GSK3β/Nrf2 signaling pathway modulated erastin-induced

ferroptosis in breast cancer. Mol Cell Biochem 2020; 473:217–228.
22. Martin SA, Souder DC, Miller KN, et al. GSK3β regulates brain energy metabolism. Cell Rep 2018;23:1922–1931.e4.
23. Khoury M, Guo Q, Furuta K, et al. Glycogen synthase kinase 3 activity enhances liver inflammation in MASH. JHEP Reports 2024;6:101073.
24. Ibrahim SH, Hirsova P, Malhi H, Gores GJ. Animal models of nonalcoholic steatohepatitis: eat, delete, and inflame. Dig Dis Sci 2016;61:1325–1336.
25. Krishnan A, Abdullah TS, Mounajjed T, et al. A longitudinal study of whole body, tissue, and cellular physiology in a mouse model of fibrosing NASH with high fidelity to the human condition. Am J Physiol Gastrointest Liver Physiol 2017;312:G666–G680.
26. Gutierrez Sanchez LH, Tomita K, Guo Q, et al. Perinatal nutritional reprogramming of the epigenome promotes subsequent development of nonalcoholic steatohepatitis. Hepatol Commun 2018;2:1493–1512.
27. Furuta K, Guo QQ, Pavelko KD, et al. Lipid-induced endothelial vascular cell adhesion molecule 1 promotes nonalcoholic steatohepatitis pathogenesis. J Clin Invest 2021;131:e143690.
28. Matsumoto M, Hada N, Sakamaki Y, et al. An improved mouse model that rapidly develops fibrosis in non-alcoholic steatohepatitis. Int J Exp Pathol 2013; 94:93–103.
29. Colletti M, Cicchini C, Conigliaro A, et al. Convergence of Wnt signaling on the HNF4alpha-driven transcription in controlling liver zonation. Gastroenterology 2009; 137:660–672.
30. Turner JA, Paton EL, Van Gulick R, et al. BRAF modulates lipid use and accumulation. Cancers (Basel) 2022; 14:2110.
31. Roh YS, Kim JW, Park S, et al. Toll-like receptor-7 signaling promotes nonalcoholic steatohepatitis by inhibiting regulatory T cells in mice. Am J Pathol 2018; 188:2574–2588.
32. Ben-Moshe S, Shapira Y, Moor AE, et al. Spatial sorting enables comprehensive characterization of liver zonation. Nat Metab 2019;1:899–911.
33. Zhou CC, Yang X, Hua X, et al. Hepatic NAD(+) deficiency as a therapeutic target for non-alcoholic fatty liver disease in ageing. Br J Pharmacol 2016;173:2352–2368.
34. Mukherjee S, Chellappa K, Moffitt A, et al. Nicotinamide adenine dinucleotide biosynthesis promotes liver regeneration. Hepatology 2017;65:616–630.
35. Chen W, Zhao H, Li Y. Mitochondrial dynamics in health and disease: mechanisms and potential targets. Signal Transduct Target Ther 2023;8:333.
36. Parlakgül G, Pang S, Artico LL, et al. Spatial mapping of hepatic ER and mitochondria architecture reveals zonated remodeling in fasting and obesity. Nat Commun 2024;15:3982.
37. Kien B, Kolleritsch S, Kunowska N, et al. Lipid droplet-mitochondria coupling via perilipin 5 augments respiratory capacity but is dispensable for FA oxidation. J Lipid Res 2022;63:100172.
38. Castro JP, Jung T, Grune T, Siems W. 4-Hydroxynonenal (HNE) modified proteins in metabolic diseases. Free Radic Biol Med 2017;111:309–315.
39. Zhang H, Lyn N, Haghani A, Forman HJ. Detection of HNE modification of proteins in aging mouse tissues: a Western blot-based approach. Methods Mol Biol 2020; 2144:237–244.
40. Cui S, Ghai A, Deng Y, et al. Identification of hyperoxidized PRDX3 as a ferroptosis marker reveals ferroptotic damage in chronic liver diseases. Mol Cell 2023; 83:3931–3939.e5.
41. Bersuker K, Hendricks JM, Li Z, et al. The CoQ oxidoreductase FSP1 acts parallel to GPX4 to inhibit ferroptosis. Nature 2019;575:688–692.
42. Nakamura T, Hipp C, Santos Dias Mourão A, et al. Phase separation of FSP1 promotes ferroptosis. Nature 2023;619:371–377.
43. Lange M, Wölk M, Doubravsky CE, et al. FSP1-mediated lipid droplet quality control prevents neutral lipid peroxidation and ferroptosis. bioRxiv 2025.
44. Xia Y, Wang Y, Xiong Q, et al. Neutrophil extracellular traps promote MASH fibrosis by metabolic reprogramming of HSC. Hepatology 2025;81:947–961.
45. Juhaszova M, Zorov DB, Kim SH, et al. Glycogen synthase kinase-3beta mediates convergence of protection signaling to inhibit the mitochondrial permeability transition pore. J Clin Invest 2004;113:1535–1549.
46. Garcia-Martinez I, Santoro N, Chen Y, et al. Hepatocyte mitochondrial DNA drives nonalcoholic steatohepatitis by activation of TLR9. J Clin Invest 2016;126:859–864.
47. Peleman C, Francque S, Berghe TV. Emerging role of ferroptosis in metabolic dysfunction-associated steatotic liver disease: revisiting hepatic lipid peroxidation. EBioMedicine 2024;102:105088.
48. Wang H, Liu C, Zhao Y, Gao G. Mitochondria regulation in ferroptosis. Eur J Cell Biol 2020;99:151058.
49. Gao M, Yi J, Zhu J, et al. Role of mitochondria in ferroptosis. Mol Cell 2019;73:354–363.e3.
50. Dixon SJ, Olzmann JA. The cell biology of ferroptosis. Nat Rev Mol Cell Biol 2024;25:424–442.
51. Mao C, Liu X, Zhang Y, et al. DHODH-mediated ferroptosis defence is a targetable vulnerability in cancer. Nature 2021;593:586–590.
52. Wu S, Mao C, Kondiparthi L, et al. A ferroptosis defense mechanism mediated by glycerol-3-phosphate dehydrogenase 2 in mitochondria. Proc Natl Acad Sci U S A 2022;119:e2121987119.
53. Yi J, Zhu J, Wu J, et al. Oncogenic activation of PI3K-AKT-mTOR signaling suppresses ferroptosis via SREBP-mediated lipogenesis. Proc Natl Acad Sci U S A 2020;117:31189–31197.
54. Demuynck R, Efimova I, Naessens F, Krysko DV. Immunogenic ferroptosis and where to find it? J Immunother Cancer 2021;9:e003430.
55. Tang D, Kepp O, Kroemer G. Ferroptosis becomes immunogenic: implications for anticancer treatments. Oncoimmunology 2020;10:1862949.
56. An P, Wei LL, Zhao S, et al. Hepatocyte mitochondria-derived danger signals directly activate hepatic stellate

cells and drive progression of liver fibrosis. Nat Commun 2020;11:2362.
57. Weisend CM, Kundert JA, Suvorova ES, et al. Cre activity in fetal albCre mouse hepatocytes: utility for developmental studies. Genesis 2009;47:789–792.
58. Hoeflich KP, Luo J, Rubie EA, et al. Requirement for glycogen synthase kinase-3beta in cell survival and NF-kappaB activation. Nature 2000;406:86–90.
59. Patel S, Doble BW, MacAulay K, et al. Tissue-specific role of glycogen synthase kinase 3beta in glucose homeostasis and insulin action. Mol Cell Biol 2008; 28:6314–6328.
60. Ibrahim SH, Hirsova P, Tomita K, et al. Mixed lineage kinase 3 mediates release of C-X-C motif ligand 10-bearing chemotactic extracellular vesicles from lipotoxic hepatocytes. Hepatology 2016;63:731–744.
61. Guo Q, Furuta K, Lucien F, et al. Integrin beta1-enriched extracellular vesicles mediate monocyte adhesion and promote liver inflammation in murine NASH. J Hepatol 2019;71:1193–1205.
62. Singer K, Maley N, Mergian T, et al. Differences in hematopoietic stem cells contribute to sexually dimorphic inflammatory responses to high fat diet-induced obesity. J Biol Chem 2015;290:13250–13262.
63. Dakin RS, Walker BR, Seckl JR, et al. Estrogens protect male mice from obesity complications and influence glucocorticoid metabolism. Int J Obes (Lond) 2015; 39:1539–1547.
64. Li J, Liu H, Mauer AS, et al. Characterization of cellular sources and circulating levels of extracellular vesicles in a dietary murine model of nonalcoholic steatohepatitis. Hepatol Commun 2019;3:1235–1249.
65. Chu DT, Malinowska E, Jura M, Kozak LP. C57BL/6J mice as a polygenic developmental model of diet-induced obesity. Physiol Rep 2017;5:e13093.
66. Guo Q, Furuta K, Aly A, Ibrahim SH. Isolation and characterization of mouse primary liver sinusoidal endothelial cells. J Vis Exp 2021;178:63062.
67. Kleiner DE, Brunt EM, Van Natta M, et al. Nonalcoholic Steatohepatitis Clinical Research Network. Design and validation of a histological scoring system for nonalcoholic fatty liver disease. Hepatology 2005; 41:1313–1321.
68. Tomita K, Kohli R, MacLaurin BL, et al. Mixed-lineage kinase 3 pharmacological inhibition attenuates murine nonalcoholic steatohepatitis. JCI Insight 2017;2:e94488.
69. Bankhead P, Loughrey MB, Fernández JA, et al. QuPath: open source software for digital pathology image analysis. Sci Rep 2017;7:16878.
70. Bradski G. Dr. Dobb's Journal of Software Tools. The OpenCV Library 2000;120:122–125.
71. Persson XM, Blachnio-Zabielska AU, Jensen MD. Rapid measurement of plasma free fatty acid concentration and isotopic enrichment using LC/MS. J Lipid Res 2010; 51:2761–2765.

Received March 12, 2025. Accepted September 11, 2025.

Correspondence
Address correspondence to: Samar H. Ibrahim, MBChB, Professor of Pediatrics and Physiology, Division of Pediatric Gastroenterology, Department of Pediatric and Adolescent Medicine, Mayo Clinic, 200 First Street SW, Rochester, Minnesota 55905. e-mail: ibrahim.samar@mayo.edu; tel: (507) 266-0114.

CRediT Authorship Contributions

Khaled Warasnhe, MD (Data curation: Lead; Formal analysis: Lead; Methodology: Lead; Writing – original draft: Lead; Writing – review & editing: Lead)

Akitoshi Sano, MD, PhD (Data curation: Supporting; Formal analysis: Supporting; Writing – review & editing: Supporting)

Qianqian Guo (Data curation: Supporting; Formal analysis: Supporting; Methodology: Supporting; Writing – original draft: Supporting; Writing – review & editing: Supporting)

Nantawat Satthawiwat (Data curation: Supporting; Writing – review & editing: Supporting)

Xin Dai (Data curation: Supporting)

Peyton A. Classon (Data curation: Supporting)

Chady Meroueh, MD (Formal analysis: Equal; Software: Lead; Writing – review & editing: Supporting)

Hyun Se Kim Lee (Data curation: Supporting)

Lucía Valenzuela-Pérez, DVM, PhD (Data curation: Supporting)

Stella Victorelli, PhD (Formal analysis: Supporting; Methodology: Supporting)

Adebowale O. Bamidele, PhD (Formal analysis: Supporting; Methodology: Supporting; Writing – review & editing: Supporting)

Petra Hirsova, PharmD, PhD (Formal analysis: Supporting; Methodology: Supporting; Writing – review & editing: Supporting)

Davide Povero, PhD (Conceptualization: Supporting; Data curation: Supporting; Formal analysis: Supporting; Methodology: Supporting; Writing – review & editing: Supporting)

Samar H. Ibrahim, MBChB (Conceptualization: Lead; Data curation: Supporting; Formal analysis: Supporting; Funding acquisition: Lead; Resources: Lead; Supervision: Lead; Writing – original draft: Lead; Writing – review & editing: Lead)

Conflicts of interest
The authors disclose no conflicts.

Funding
This study was funded by National Institutes of Health/National Institute of Diabetes and Digestive and Kidney Diseases grants R01DK122948 (Samar H. Ibrahim), P30DK084567 (Samar H. Ibrahim), R01DK130884 (Petra Hirsova), and K01DK124358 (Adebowale O. Bamidele).